


Spring 4-13-2017

The Mathematical Theory of Deformation Arrest in Large-Strain Dynamic Plasticity

Brendan A. Kullback
University of New Mexico

Follow this and additional works at: https://digitalrepository.unm.edu/me_etds

 Part of the [Engineering Mechanics Commons](#), [Mechanical Engineering Commons](#), [Mechanics of Materials Commons](#), and the [Ordinary Differential Equations and Applied Dynamics Commons](#)

Recommended Citation

Kullback, Brendan A.. "The Mathematical Theory of Deformation Arrest in Large-Strain Dynamic Plasticity." (2017).
https://digitalrepository.unm.edu/me_etds/129

This Dissertation is brought to you for free and open access by the Engineering ETDs at UNM Digital Repository. It has been accepted for inclusion in Mechanical Engineering ETDs by an authorized administrator of UNM Digital Repository. For more information, please contact disc@unm.edu.

Brendan A. Kullback

Candidate

Mechanical Engineering

Department

This dissertation is approved, and it is acceptable in quality and form for publication:

Approved by the Dissertation Committee:

Dr. Yu-Lin Shen , Chairperson

Dr. Mehran Tehrani

Dr. Jonathon Rogers

Dr. Muhammad Hajj

The Mathematical Theory of Deformation Arrest in Large-Strain Dynamic Plasticity

by

Brendan Adam Kullback

B.S., Mechanical Engineering, University of Colorado at Colorado Springs, 2009

M.S., Engineering Mechanics, Virginia Polytechnic Institute and State University, 2012

DISSERTATION

Submitted in Partial Fulfillment of the
Requirements for the Degree of

Doctor of Philosophy
Engineering

The University of New Mexico

Albuquerque, New Mexico

May, 2017

Dedication

This dissertation is dedicated to my friend and highly esteemed mentor Mark David Carrara (April 15, 1974 to July 4, 2013).

Acknowledgments

I would like to thank my advisor Dr. Yu-Lin Shen for all his support and assistance through my stay at the University of New Mexico. Without his help, this work would not be possible. I recognize my committee members Dr. Jonathan Rogers, Dr. Mehran Tehrani, and Dr. Muhammad Hajj. For Dr. Rogers and Dr. Hajj, I am deeply grateful and indebted for your kindness and perseverance to see my success. I am thankful for all the help and inspiration I have received in my graduate studies for whom I admire, especially Dr. Guillermo Terrones and Dr. Mark David Carrara. I would like to further acknowledge all my co-workers and fellow graduate students, as well as the management at Sandia National Laboratory and Los Alamos National Laboratory for their encouragement and funding support throughout my higher education. Finally, I thank my family and friends for all their reassurances through this long process.

The Mathematical Theory of Deformation Arrest in Large-Strain Dynamic Plasticity

by

Brendan Adam Kullback

B.S., Mechanical Engineering, University of Colorado at Colorado Springs, 2009

M.S., Engineering Mechanics, Virginia Polytechnic Institute and State University, 2012

Ph.D., Engineering, University of New Mexico, 2017

Abstract

Ductile structural components subjected to explosive loadings exhibit a large range of behaviors. The response of beams, walls, and blast doors is estimated using two methods. The engineering level approaches are highly simplified and neglect much of the relevant physics while the use of finite element or shock-code simulation is expensive and not suited to rapid problem solving and parameter studies. In this dissertation, a medium fidelity reduced order modeling approach has been derived to capture the most relevant physics governing rupture of ductile bodies dynamically deforming in tension.

Solution of the inertially stretching jet is used to reveal the deformation arrest mechanics with large plastic strains and high strain-rates. This phenomenon is exemplified by applying a moving boundary technique to a rigid-plastic interface

associated with tensile flow-stress release (Mott-Lee wave). A system of differential-algebraic-equations for the axisymmetric jet is formulated for mass, momentum, and energy balances as well as constraints for kinematic compatibility. Dimensional analysis uncovers distinctive dimensionless numbers and the relationship to the plastic velocity increment found in the stability analysis for plastic jet particulation. The closed form solution process reveals underlying mechanics not realized prior. Predictive theoretical rupture conditions, plastic zone size, mass and velocity of the detached particle if rupture occurs, the time for motion to cease as well as the rupture strain are obtained. The numerical solution is in excellent agreement with both shock-code and finite-element simulations. The solution also illustrates the velocity pullback phenomena observed in prior experiments and parametric representation results for the body shape at any instant during deformation.

It is shown that isotropic homogeneous constitutive equations for plastic flow-stress can be included in the governing system of equations for deformation arrest. This is exemplified using the Johnson-Cook viscoplastic relation [37] with the addition of a plastic work to temperature rise equation. The influence of thermal softening, strain-rate stiffening, and work hardening is discussed on the behavior of the inertially stretching jet.

External and coupling loads are applied to the mathematical treatment proposed. Closed form solution is obtained to the application of a tensile step loading on the jet tip. Analysis results in the rectangular-hyperbolic relationship between loading and its impulse on the rupture threshold. The asymptote for minimum impulse at maximum loading is found to be dependent on both the jet slender ratio and kinetic energy density to yield strength ratio. The asymptote for the minimum pressure at maximum loading is found to only depend on the kinetic energy density to yield strength ratio. Drag resistance has been applied to the jet tip with little influence on jet motion unless the density of the surrounding fluid is comparable to the jet

material. Coupling the deformation arrest process for linearly stretching ductile material to a single-mode beam undergoing late-time motion with angular deflection has been accomplished. Solution results show complicated features including rupture and full arrest.

Contents

List of Figures	x
1 Introduction	1
1.1 Objectives	2
1.2 Literature Review	4
2 Methods of Computational Analysis	12
2.1 CTH	12
2.2 Abaqus	14
2.3 Mathematica DAE Solver	15
3 The Reduced Order Modeling Approach for Deformation Arrest in the Inertially Stretching Ductile Jet	16
3.1 Abstract	16
3.2 Introduction	17
3.3 ROM Formulation	19

Contents

3.3.1	Derivation	20
3.3.2	Dimensional Analysis	23
3.4	Analysis and Discussion	24
3.4.1	Rupture Conditions	25
3.4.2	Velocity Pullback Phenomena	27
3.4.3	Rupture Strain	31
3.4.4	Deformed Shape	33
3.5	Conclusions	33
4	Viscoplastic Effects on the Deformation Arrest Process	36
4.1	Abstract	36
4.2	Introduction	36
4.3	Thermal Softening	39
4.4	Strain-Rate Stiffening	44
4.5	Work Hardening	46
4.6	Combined Effects	48
4.7	Conclusions	50
5	The Application of External and Coupling Loads on Deformation Arrest in Tensile Ductile Stretching	52
5.1	Abstract	52
5.2	Introduction	53

Contents

5.3	Loading of the Tensile Jet	56
5.3.1	Step Impulse and the P-I Diagram	58
5.3.2	Closed Form Solution	59
5.4	Drag Resistance During Jet Motion	63
5.5	Stretching of the Root in Transverse Beam Deflection	65
5.6	Conclusions	69
6	Conclusions	72
6.1	Summary	73
6.2	Future Work	75
	Appendices	76
A	Example CTH Input File	77
B	Example CTH Output Data Analysis Code	82
C	Example Abaqus Keyword Input	86
D	Example Abaqus-Python Output Analysis Code	93
E	Example Mathematica DAE Solver	96
	References	98

List of Figures

3.1	Inertially stretching jet illustration with representative flow stress and velocity profiles	21
3.2	CTH simulation of the deformation arrest process with the radial velocity irregularity highlighted on the right. The left is the corresponding the von Misses effective stress profile.	22
3.3	Dimensionless release zone length	26
3.4	Dimensionless release zone mass	28
3.5	Velocity of the jet tip illustrating the velocity pullback phenomenon	29
3.6	Dimensionless plastic zone strain rate	30
3.7	Dimensionless jet cross section	31
3.8	Dimensionless plastic zone length	32
3.9	Release Zone contour during deformation arrest for a non-rupturing jet	34
3.10	Release Zone contour during deformation arrest for a rupturing jet .	35

List of Figures

4.1	Inertially stretching jet illustration with representative flow stress and velocity profiles	38
4.2	Influence of N_T and m on the homologous temperature as a function of time	42
4.3	Homologous temperature profile along the jet length at several instances in time	43
4.4	Inertially stretching jet illustration with representative flow stress and velocity profiles with strain-rate stiffening	44
4.5	Comparison of Abaqus simulation with the numerical DAE solutions for strain-rate stiffening shown with the strain-rate shift and the perfectly plastic reference case where $Y = 1$	45
4.6	Comparison of Abaqus simulation with the numerical DAE solutions for work hardening shown with the perfectly plastic reference case where $Y = 1$	47
4.7	Comparison of Abaqus simulation with the numerical DAE solutions with combined viscoplastic effects shown with the perfectly plastic reference case where $Y = 1$	49
5.1	Inertially stretching jet illustration with representative flow stress and velocity profiles	54
5.2	Inertially stretching jet illustration with representative flow stress and velocity profiles with a tensile load	57
5.3	Solution comparison of the ductile jet with a tensile step loading . .	62
5.4	P-I relationship for a step impulse on the rupture threshold	63

List of Figures

5.5	Solution of the inertial jet with drag resistance	64
5.6	Illustration of an single mode beam in phase 3 with tensile stretching at the root	66
5.7	Kinetic free-body diagram of an single mode beam with coupling action applied to the root	66
5.8	Solution of deflecting beam motion fully arresting	69
5.9	Solution of deflecting beam with rupture at the root	70

Chapter 1

Introduction

Traditionally, the vulnerability of structural components such as beams, walls, and blast doors to intense explosive and impulsive loadings is estimated using highly simplified methods, neglecting much of the physics. However, the principal physical mechanisms governing the mechanics has been well studied over the last seven decades. Although there is a wealth of literature on large-strain dynamic plasticity, plastic buckling, fragmentation, particulation, and rupture as well as the underlying material science, a general mathematical theory has yet to be developed.

The governing equations at the continuum scale are non-linear partial-differential equations (PDE's) which require expensive shock-codes or finite element software with intricate numerical techniques to solve. Practical problems are often multi-material and involve composite structures such as steel-concrete-steel sandwiches (SCS) for which solutions require greater computational power than available in a typical desktop computer. The large amounts of computational power required to solve even relatively simple problems is often not available or too costly for repeated calculations used to perform parametric design or assessment studies. Furthermore, internal structure details may not be known, or are yet to be determined for which

Chapter 1. Introduction

the cost of using high-fidelity software is not justified. These limitations create a need for an engineering-level mathematical model that captures the most relevant physics and matches the shock-code or finite element solutions within reasonable allowances and with limited computational cost.

An incident blast wave transfers momentum into a structure element by a physically complex series of shock-rarefaction interactions upon partial reflection and partial transmission from each internal and external surface. This induces movement and generates deformation gradients within the structure. Shock-codes are typically designed and optimized to capture these transient details which are unnecessary for calculations with low-fidelity structure detail as well as low fidelity initial and loading conditions. Generally, better suited are finite element algorithms however when material distortion becomes significant and rupture approaches, these codes often fail due to mesh entanglement or numerical instability. Physically, the deformation arrest process caused by strength induced dissipative action occurs over large timescales relative to material sound speeds. Therefore, explicit numerical solutions become costly to compute the intermediate and end structure configurations.

1.1 Objectives

The objective of this work is to formulate and validate an engineering-level mathematical theory for deformation arrest to obtain final configurations for ductile bodies subjected to impulse or blast loadings. The final state of a SCS structure or any other ductile body subjected to blast, shock, or impact loadings for which there are large distorting plastic strains is directly dependent on the initial configurations, boundary conditions, loading histories, and deformation arrest mechanics. Assuming known initial configurations, boundary conditions, and externally applied loading histories, the deformation arrest mechanics that most influences tensile rupture at the attach-

Chapter 1. Introduction

ment points is explored and a mathematical treatment developed.

The most simplistic scenario for which the deformation arrest mechanisms and tensile rupture can be identified and a mathematical treatment developed is for that of an inertially stretching jet. The inertially stretching jet, of interest in shaped charge design, explosively formed projectiles, micro-jetting, surface ejecta, dynamic extrusion, particulation, and plastic instability has been studied for many decades. Nevertheless, the deformation arrest process and resulting material dynamics has yet to be fully developed even with foundational concepts having been proposed in dated publications. The general deformation arrest process applied to tensile release also applies to compressive release. The classical Taylor-anvil impact problem for solid slugs and tubes quantitatively need not be addressed in this here. However, the modeling approach may be proposed. Likewise, jet particulation may not be quantitatively addressed, but the modeling approach may be described for future work.

When transverse loadings are applied, bending and shearing stresses are introduced. Regions of both compression and tension form in early time as plastic hinges. As deflections increase, compressive regions become tensile in nature and the same deformation arrest mechanisms are observed as those in inertially stretching jets and Taylor-anvil impact studies. Analogously with the inertial jet, the tensile rupture process ensues as plastic hinges are stretched. The analysis method formulated for the jet can be coupled with appropriate modification to include attached bodies in bending and shearing. This mathematical treatment may unify traditional approaches for structural dynamic plasticity and crashworthiness with co-linear plastic instability, particulation, and the higher strain-rate phenomena. When structures become multi-material sandwiches, the deformation and deformation arrest process becomes much more complex.

1.2 Literature Review

To formulate a physics based engineering approach to analyze multiplex deformable structure-blast vulnerability and design scenarios, problems of ordinary geometric bodies with simplistic loadings are examined. Dynamic problems in large strain dynamic plasticity where tensile plastic release and plastic compressive loading waves are the dominant effect as well as plastic hinges where transverse deformation governs the structural response are reviewed. These problems share important underlying physical mechanisms which are highlighted in this section.

After the conclusion of World War II, N.F. Mott proposed the foundational concepts for the deformation arrest mechanism [63]. This was done in support of a statistical distribution developed for fragment size in exploding bomb shells and casings. It was expressed that a tensile stress release-wave propagates into plastically elongating metal separating a no-longer deforming region from the rest of the deforming body. The no-longer deforming region is postulated to behave in an elastic manner, treated as a rigid body with respect to the total strain. This rigid zone is where the effective stress state has dropped below the plastic flow stress. The release-wave would originate from a point of instantaneous fracture where defects occur. For the scenario of a rapidly expanding shell, it was assumed that the stress release to fracture process occurs at a time scale much smaller than the bulk motion of the metal. Therefore, it was assumed that the metal thickness, strain-rate, and flow stress can be treated as constants. A momentum balance applied across the release-wave/interface lead to a straightforward analytical solution for the plastic boundary location relative to an originating crack and the tangential motion of the release zone as a function of time. A wealth of publications has resulted from this report to estimate fracture initiation and the statistics for example, see the textbook by Grady [25]. However relatively limited development into an engineering formulation for the deformation arrest process has ensued. Lee [50] solved for the elastic-plastic solution

Chapter 1. Introduction

using characteristic methods to Mott's propagating tensile release-wave with equivalent results. This report will use the term Mott-Lee wave to be consistent with the academic literature. Many authors have also studied the elastic-plastic release wave for various material and other geometric bodies [5, 14, 15, 19, 28, 70, 72, 77, 78, 89]. It was noted by Grady [25] that the tensile release process was wave-like initially but then behaved in a diffusive manner, therefore solved the same problem with a diffusion solution also with equivalent results. Grady et. al. [26] and Kipp and Grady [48] proposed that energy dissipated at the moment of the initiating fracture had an ensuing effect which was assumed to be negligible prior. The dissipated energy at fracture was treated as occurring from a linear elastic resistance function applied to the free end of the fracture. Noteworthy experimental work was performed by Zhang and Chandar [107, 108] who observed the formation of complete and incomplete (local necking) fracture sites. The observations made matched that predicted by Grady [25] including the tangential motion of the release zone. The fracture of rapidly expanding shells has been studied by [21, 24] and others.

The idea of the Mott-Lee release wave has also been linked to necking and particulation phenomena in ductile materials. Walsh [91] recognized that for shaped charge jets, the Mott-Lee wave propagates from an adjacent region within the jet from where variation in the cross-sectional area was large enough for flow stress relief. For the conditions where the cross-section area changes as the release wave propagates, it was elucidated that the shape of jet particulate could therefore be calculated. However, the shape calculation was not developed and was not performed. The release wave was postulated to propagate quickly over short distances but slowly over long distances, thereby limiting the range of influence in very high strain-rate shaped charge jets. The velocity increment between particulate after jet breakup was found to be intimately related to the flow-stress release process by Hirsch [33] and expressed through the evolution of microscopic adiabatic shear bands and kinetic energy dissipation. The formation of microscopic adiabatic shear bands in dynamic

Chapter 1. Introduction

stretching is well studied topic on its own within the material science perspective of dynamic plasticity [90] as well as martensitic transformation [105]. Jet particulation has been well analyzed with respect to perturbation stability [8, 9, 69, 73, 83, 99, 109] and many other authors.

Due to the high velocities and sensitivity to random perturbation in shaped charge jets, the arresting mechanics are hard to observe in experiment. Therefore, dynamic extrusion experiments where a ductile projectile is shot into a converging nozzle-like dye and exiting as an elongating jet, provide more direct insight. Trujillo et al. [88] observed a velocity pullback phenomenon while conducting photonic Doppler velocimetry experiments to measure the jet speed. As the projectile enters the dye, the projectile material accelerates as it deforms. As the material leaves the die, the formed jet decelerates until necking and particulation occurs, finally traveling at a constant velocity when the deformation has ceased. While almost all the dynamic tensile extrusion literature regards the texturing and crystal material science, Cao et al. [11] reported that the projectile material arrested within the die had its crystals increasingly elongated from the dye entrance to the exit where necking had ensued. Numerical simulation by Bonora et al. [10] and Gray et al. [27] showed total plastic strain profiles that were non-uniform with larger plastic strains where necking had occurred prior to arrest.

Rigid-Plastic boundary propagation is also fundamental in the analysis and modeling of dynamic plasticity problems where the dominant stresses are compressive. The problem of a metallic slug impacted onto a rigid boundary was first reported by G. I. Taylor [81]. Taylor expressed that upon impact, an elastic-plastic wave boundary propagates into the un-deformed slug tail from the impact surface. A force-acceleration balance was applied across the rigid-plastic boundary, roughly approximating the motion of the un-deformed slug tail as well as the final shape near the impacted surface. Wiffin [95] then used Taylor's work to compute the dynamic yield

Chapter 1. Introduction

stress of several materials from experiment. Lee and Tupper [51] performed the analogous elastic-plastic momentum balance which resulted in an improvement only at very small impact speeds and Phillips et al. [70] analyzed this elastic-plastic problem with a variably changing cross section. Motivated to develop and refine flow-stress archetypes, numerous efforts to capture the motions and deformed slug shape have been made to Taylor's original work with varying amounts of success. Hawkyard [30] and Hawkyard et al. [31] applied an energy balance across the plastic wave front which resulted in a slightly improved approximation and capturing a more realistic final slug shape near the impact surface. Jones et al. [42] proposed the need to use a mass accretion-like momentum balance across the rigid-plastic boundary to account for mass transfer from the rigid to the plastic zone while Jones and Gillis [43] derived scaling rules for the boundary propagation. A series of publications from Jones and collaborators [44, 45, 46, 41] undertook thorough development for an engineering formulation, termed the $\alpha\beta$ model. The mass-accretion momentum balance was applied with different rule sets based on three distinct phases of plastic boundary motion and assumptions about the material velocity jump across this boundary. House et al. [35] applied an approximation to the $\alpha\beta$ model to reduce the difficulty of solution and was modified by Eakins and Thadhani [20] for the reverse case of an anvil impacting a stationary slug while suggesting limitations on the accuracy of the three-phase approach. The need to include additional kinetic dissipating terms, as opposed to only the compressive work-energy previously considered was proposed by Woodward et al. [97]. Foster et al. [23] applied a traditional shock discontinuity treatment for the plastic wave propagation resulting in a solution consistent with the $\alpha\beta$ model. In the past few years, an attempt to formulate a closed-form solution in terms of elementary functions while improving experimental correlation was performed by Wlodarczyk et al. [96]. Once again, an energy based approach was attempted by Dastjerdi et al. [18] to more correctly match the deformed slug profile. Most recently, simulations performed by Chakraborty et al. [13] exhibited a non-zero, non-uniform material ve-

Chapter 1. Introduction

locity profile in the plastic zone. Therefore, a mathematical formulation to include this behavior was presented with much improvement upon the un-deformed segment motion and the plastic zone dimensions.

Dynamic plastic buckling where both characteristics of the Taylor-anvil impact and that of buckling are observed simultaneously also provides insight. Experimental and finite element simulations performed by Wang and Lu [93] demonstrate a transition from the Taylor-anvil-like “mushrooming” shape profile to that of plastic buckling-like “wrinkling” and then to that of progressive buckling “folding”. It was shown that as the tube wall increases in thickness and the impact speed increases, the mushrooming effect has a reduced ability to stabilize the wrinkling and folding behaviors. Thin tubes with lower impact speeds resulted in more progressive folding that gradually transitions to mushrooming with wrinkling for medium sized tube walls and intermediate impact speeds and then to Taylor-anvil-like shaping with the thickest tubing and the highest speeds.

Permanent beam deflection due to impulse and impact loadings is a well-developed topic [40, 102] however, a complete description for the rupture conditions is yet to be realized. The complexity of the problem was highlighted by Menkes and Opat [62] who experimentally applied pulse loads of increasing intensities to clamped beams. Three failure modes were identified: Mode I - large permanent deformation without rupture, Mode II - large permanent deformation with tensile rupture, and Mode III - shearing rupture at the supports with little center-point deflection. Several approaches have been proposed to predict the mode I - II and mode II - III transition criterion. The founding approach defines a strain-to-rupture condition [39]. In this scheme, rupture is said to occur when the plastic strains induced at the plastic hinges reaches a material specific nominal rupture strain. However, the plastic strains within the hinge are directly affected by the poorly characterized plastic zone volume at the hinge. Shen and Jones [74] sought to generalize the strain-to-fail approach by proposing that rupture occurs instead when the structures initial kinetic energy

Chapter 1. Introduction

exceeds a maximum capacity of dissipated energy via plastic work. Even though work hardening and strain-rate stiffening can be included, a strain-to-failure property is still needed and the ill-defined plastic zone volume required. Li [53] related this condition to other classical fracture processes through a continuum mechanics analysis. Zhao [110] proposed using critical values of Johnson's damage number [38], $\mathcal{D} \equiv \rho u_0^2 / \sigma_y$ where ρ is the density, u_0 the initial structure velocity calculated from the applied impulse, and σ_y the yield strength to predict shear rupture like the Reynolds number for turbulent flow transition. These theories have been reviewed in multiple reports and texts, for example [101]. Plastic hinge formation has been well studied for the development of segmented deflection calculations, standardizing a three-phase analysis. The interaction of bending, tensile, and shearing yield surfaces in the forming of plastic hinges has been subsequently analyzed [6, 32, 34, 47, 52, 64, 65, 66, 80] and is reviewed in several textbooks as well [40, 58, 79].

Analogous response characterization, Mode I, II, and III are observed in impulsively loaded plates and shells [67, 68, 71, 84]. Shen and Jones [75] reported good agreement using the maximum plastic work condition for deflection in Mode I, but poor agreement for predicting Mode II and Mode III rupture conditions on circular plates. Smith and Nurick [84] observed an inward radial motion during deformation causing stretch at the boundary. Zaera et al. [104] included inertia terms not previously applied to the yield condition and reported improved results while Zajkani et al. [106] analyzed multiple hinges within the plate. The strain-to-rupture condition was also obtained by Wen [94] considering work hardening for circular plates and reported that rectangular plates can be reasonably approximated as circular plates. Higher resolution experiments by Nurick and Shave [67] however found a more complex combination of Mode I and Mode II conditions at different edge boundaries as well as inward tensile pulling and local necking prior to rupture for rectangular plates. Langdon and Schleyer [49] devised an approach to treat the plastic line-hinges at the boundaries with the strain-to-rupture condition. The size of the plastic

Chapter 1. Introduction

hinge used in their analytical calculation however was measured a-priori from their experiments. A dimensionless response number was derived by Zhao [111] defined as $\mathcal{R} \equiv \mathcal{D}(l_0/\delta_0)^2$ where \mathcal{D} is the Johnson damage number, l_0 and δ_0 are characteristic in-plane and transverse length measurements respectively. Hu [36] recast circular and rectangular plate deflections from various authors into functional forms of \mathcal{R} while Li and Jones [54] suggested additional numbers need to be included in the dimensional analysis when transverse shear, work hardening, strain-rate stiffening, and thermal softening is included. Shi and Gao [76] recognized that Zhao's response number can be generalized to characterize the effects on other geometric bodies. The generalized number is defined as $\mathcal{R}_n \equiv \mathcal{D}(l_0/\delta_0)^n$ where n is a positive real number. It was also suggested that the dynamic elastic behavior as well as plastic and elastic buckling can be represented with the appropriate replacement for \mathcal{D} . Yao et al. [100] recast \mathcal{R}_n into a form using the experimentally measured quantities, explosive mass and standoff distance. It is important to recognize that all the mentioned theoretical analysis consider only application of an ideal impulse. The analysis methods treat the structures as deforming inertially with prescribe initial velocity profiles calculated from elementary impulse-momentum relationships. Early time acceleration phase of the structures is neglected.

Sandwich structures with compressible cores such as foams or honeycombs have received generous attention due to their blast and impact mitigation properties. These structures have large energy absorption capacity [3, 103, 112] but with rupture conditions still not well predicted. The deflection and rupture behavior of sandwich structures with incompressible cores is not as well characterized. Several numerical and experimental studies have been performed [7, 86, 87] showing tensile fracturing of the concrete with bending and localized buckling on some cases for the steel in compressive zones. Wang et al. [92] developed a single degree-of-freedom approach to estimate the center deflection of a blast loaded SCS wall. Other work experimentally tests shear connectors to prevent separation of the steel from the

Chapter 1. Introduction

concrete [57]. Concrete filled steel tubes (CFST) have been well studied for static loadings but dynamic transverse loadings have limited publications [16, 58]. Reinforced concrete however behaves differently than confined concrete largely due to spalling phenomenon [12, 16, 85, 98] and brittle characteristics.

Chapter 2

Methods of Computational Analysis

In this chapter, a summary of the computational tools used to validate the proposed reduced-order approach is provided. Each of the computational tools are highly complex with decades of development. This chapter is intended to provide a brief background to the simulation programs and how they are used in this study. This is not a comprehensive description or examination of the software and their full capabilities.

2.1 CTH

The finite volume shock-code chosen in this study to validate the proposed mathematical theory is CTH [17]. CTH is a Sandia National Laboratory produced and distributed software packaged optimized to simulate multi-material, compressible, large-strain, high strain-rate mechanics often because of high speed impact or explosive loadings. The materials are inserted into an Eulerian grid with user assigned

Chapter 2. Methods of Computational Analysis

equation of state and constitutive models. During simulation, material flows through the grid with each cell accounting for the material volume fractions and state (density, pressure, temperature, stress tensor, flow stress, velocity vector, etc.). When the volume fraction drops below a cutoff threshold, the material has flowed out of that cells' region in space.

Many constitutive model options are available, many with progressive damage and empirical fracture conditions. In this study, rupture conditions are sought based only on conservation laws restricting the constitutive model implemented to only perfectly plastic and viscoplastic treatments. A tabular equation of state is chosen from the SESAME database to best represent real material. During deformation arrest, pressure variations from ambient are small, the materials have low compressibility and therefore largely insensitive to the equation of state details. Grid spacing is chosen small enough that the quantities of interest extracted from the simulation results are converged.

Since CTH is optimally designed for impact and explosive loading simulations, it is not well suited for the user to have high initial condition control with deforming material at zero-time. To obtain the desired initial conditions, several unique features of the software packaged are implemented. A user option for an initial linear velocity gradient is applied along the jet axis. At zero-time however, this causes an impulsive collapse in the radial direction producing a compressive wave that interferes with the deformation arrest process. Since CTH is designed to simulate shock waves and compressible flow phenomena in solids, this compressive wave dissipates after some time. Once the transient effects have decayed, a material discard feature is used to remove the jet tip material and create a sudden stress free condition on a new jet tip on an unperturbed portion of the jet. Since strains and temperature rise are non-zero at time of discard, viscoplastic effects are difficult to isolate.

There is also limited user control over boundary conditions. Since the behavior

of the jet tip to the sudden stress free condition is desired, the root of the jet meets a reflective boundary to create a zero material velocity condition in the axial direction without addition stress release. If the radial motion of the jet at the boundary is restricted, additional points of stress release occur that influence the behavior of the jet tip. As the stress release from the jet tip approach the boundary, the simulations are terminated due to boundary interference. An example input file is given in Appendix A.

At prescribed time intervals, the material state in each cell in the computational domain is written to disk. A custom script then reads these files and extracts the quantities of interest by looping through and searching for cells with certain material states. When the desired states are found, maximums, minimums, and averages are obtained over the body and then output for analysis. An example script for data extraction is given in Appendix B.

2.2 Abaqus

In addition to the shock-code, the commercial finite-element software package Abaqus [1] is used for validation. Time integration is done in Abaqus-Explicit over a Lagrangian mesh attached to an incompressible material body. Material properties (density, temperature, yield stress, etc.) are assigned with an axial velocity gradient and uniform initial temperature. Mesh size is chosen small enough that the extracted quantities are converged.

An initial radial velocity is internally computed to conserve element volume. In the finite element formulation, material cannot rupture due to conservation laws alone. Empirical damage and fracture conditions with element removal must be implemented otherwise distortions become very large and numerical failure occurs. This tool can be used however for early time approaching rupture but not for determining

rupture itself.

Greater control over boundary conditions allow arbitrary functions for pressure be applied to the material surface and viscoplastic analysis can have zero initial strains and temperature rise. Boundary at the root is restricted by direct specification to have a zero axial velocity. An example of an input keyword set used in given in Appendix C. The material state in each element is saved at selected time intervals and read by a custom script to extract the quantities of interest in the same manner done with CTH and output of analysis. An example of this script is given in Appendix D.

2.3 Mathematica DAE Solver

To solve systems of Differential Algebraic Equations (DAE's), the NDSolve function in the commercial analysis tool Mathematica [61] is utilized. When NDSolve is called, the function converts the input into an explicit form, checks the system for consistent initial conditions and algebraically solves for any unspecified values. The Implicit Differential-Algebraic (IDA) algorithm is then evoked, employing a combination of backward differentiation formula. The equations are numerically integrated using Newtonian forward-time integration approaches. Further details are available in the Mathematica documentation with a wealth of references to the numerical theory. An example of the DAE input and solver code is given in Appendix E.

Chapter 3

The Reduced Order Modeling Approach for Deformation Arrest in the Inertially Stretching Ductile Jet

3.1 Abstract

A reduced order modeling approach has been applied to the inertially stretching ductile jet revealing the deformation arrest mechanics in dynamically deforming ductile bodies with large plastic strains. This phenomenon is exemplified by applying a moving boundary technique to a rigid-plastic interface associated with tensile flow-stress release (Mott-Lee wave). A system of differential-algebraic-equations for the axisymmetric problem is formulated for mass, momentum, and energy balances as well as constraints for kinematic compatibility. Dimensional analysis uncovers distinctive number groupings and the relationship to the plastic velocity increment found in

the stability analysis for plastic jet particulation. The closed form solution process reveals underlying mechanics not realized prior. Predictive theoretical rupture conditions, plastic zone size, mass and velocity of the detached particle if rupture occurs, the time for motion to cease as well as the rupture strain is obtained. The numerical solution is in excellent agreement with both shock-code and finite-element simulations. The solution also illustrates the velocity pullback phenomena observed in prior experiments and parametric representation results for the body shape at any instant during deformation.

3.2 Introduction

Deformation arrest leading to ductile rupture of structural components subjected to explosive loadings has proven to be a challenging problem. Solutions require complex finite-element or finite-difference methods to numerically integrate the Cauchy momentum equation simultaneously with the continuity and thermodynamics equations as well as constitutive and state models. The principal physical mechanisms have been discussed over the last seven decades but a predictive reduced order model (ROM) approach has yet to be developed. In this paper, such an approach is illustrated for the simplest of geometries, the co-linear stretching ductile jet subjected to tensile release.

The inertially stretching ductile jet has been studied since the 1940's due to its inherent penetrability into dense materials as a coherent stream. Consequently, the conditions for jet breakup into a cascade of small particulate has also been analyzed as it relates to perturbations leading to plastic instability. Walsh [91] recognized that for shaped charge jets undergoing breakup, a flow stress release process occurs at late time. The flow stress release process is associated with plastic deformation arrest and is known as the Mott-Lee wave [25]. The Mott-Lee wave propagates from

an adjacent region within the jet from where variation in the cross-sectional area was large enough for stress reduction. For the conditions where the cross-sectional area changes on the same time scale as the release wave propagation, Walsh [91] elucidated that the shape of the jet particulate could be predicted. It was noted that the release wave propagates quickly over short distances but slowly over long distances, thereby limiting the range of influence in the extreme strain-rate regime under discussion. The shape calculation was therefore not developed. However, the velocity increment between particulate after jet breakup was found to be intimately related to the flow-stress release process by Hirsch [33] and expressed through the evolution of microscopic adiabatic shear bands and mechanical energy dissipation via internal plastic work.

The Mott-Lee wave propagation has been foundational in developing statistical distributions for fragment size in exploding bomb shells and casings [63]. It was expressed by Mott [63] that a tensile stress release-wave propagates into plastically elongating metal separating an elastic region from the plastically deforming body. In the elastic region, the stress state has decreased below that required for continued plastic flow. The elastic strains are neglected due to dominating plastic strains, therefore rigid body motion is assumed in the elastic regions. The release-wave would originate from a point of instantaneous fracture where metallurgical defects exist. For the scenario of a rapidly expanding shell, it was assumed that the stress release to fracture process occurs at a time scale much smaller than the bulk motion of the metal. Thus, it was assumed that the metal thickness, strain-rate, and flow stress can be treated as constants. A momentum balanced applied across the release-wave lead to a straightforward analytical solution for the plastic boundary location relative to an originating crack and the tangential motion of the release zone as a function of time. It was noted by Grady [25] that the tensile release process was wave-like initially but then behaved in a diffusive manner and solved the same problem with a diffusion solution with equivalent results. Lee [50] solved for the elastic-plastic

solution using characteristic methods to Mott’s propagating tensile release-wave also with equivalent results.

Grady [25] presents various statistical models for fragment sizes based on Mott’s original analysis. Additional analytic work aided improvements to the statistical fragment size models by analyzing fracture initiation [26, 48]. Experiments by Zhang and Chandar [107, 108] observed the formation of complete and incomplete (local necking) fracture sites. These observations matched those predicted by Grady [25] and Mott [63] including the tangential motion of the release zone.

Dynamic extrusion experiments in which ductile projectiles are shot via gas gun into a converging nozzle-like dye and exiting as an elongating jet, provides insight into deformation arrest mechanics. Trujillo et al. [88] observed a velocity pullback phenomenon while conducting experiments to measure the jet speed. As the projectile enters the dye, the projectile material accelerates as it deforms and flows through the dye. As the material leaves the dye, the formed jet decelerates until necking and particulation occurs. While almost all the dynamic tensile extrusion literature regards the texturing and crystal material science, Cao et al. [11] reported that the projectile material arrested within the die had its crystals increasingly elongated from the dye entrance to the exit where necking had ensued. Numerical simulation by Bonora et al. [10] and Gray et al. [27] showed total plastic strain profiles that were non-uniform with larger plastic strains where necking had occurred prior to arrest. These reports establish a physical basis for the ensuing mathematical formulation.

3.3 ROM Formulation

A reduced order model (ROM) for the deformation arrest process is hereby formulated for an inertially stretching ductile jet.

3.3.1 Derivation

Consider the jet of a ductile material in Figure 4.1 with constant uniform density ρ . The perfectly plastic flow stress is σ_Y . At time $t = 0$, the jet has cross section δ_0 , strain rate ε'_0 and length l_0 that evolve in time as $\delta(t)$, $\varepsilon'(t)$ and $l(t) + \xi(t)$, respectively. At this instant, the jet tip moving with velocity u_0 is released, allowing propagation of the Mott-Lee wave. The region in which the internal stress has released will have a length $\xi(t)$ as measured from the jet tip for which the material moves with velocity $u(t)$. This divides the jet into a plastic region and elastic region separated by an interface located at a distance $l(t)$ from the root. The interface is assumed to be planer as well as perpendicular to the axis of symmetry. The plastic region maintains a uniform cross section. Our simulations show that for moderate ε'_0 up to shortly after that required for first rupture, these assumptions are reasonable. Our simulations suggest that curvature of this interface causes a small axial velocity disparity. Either voids must form or the radial velocities in the plastic zone adjacent to the interface must be accelerated to maintain continuity. The latter of which is illustrated in Figure 3.2 by CTH simulation. For larger ε'_0 , the interface curvature is significant and propagation of which causes a local reduced radius. Convexity in radii profile induces additional release zones to form. Interaction of multiple release zones then leads to particulation as the jet axial velocity profile undergoes discretization.

An analogy will be drawn with moving boundary approaches in solidification processes. As the rigid-plastic interface propagates into the plastic region during unloading, the material crossing this boundary is no longer allowed to deform as that material binds with the rest of the rigid region. The shape of the rigid region can therefore be obtained by parametric representation. The mass accretion rule for the rigid region as shown in Figure 4.1 is

$$\frac{dm}{dt} = \rho \delta \frac{d\xi}{dt} \tag{3.1}$$

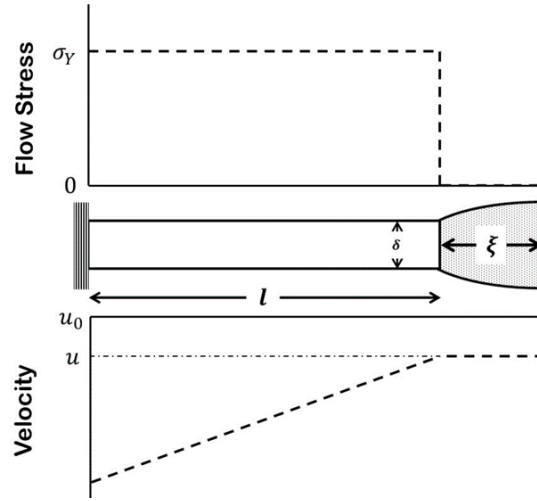


Figure 3.1: Inertially stretching jet illustration with representative flow stress and velocity profiles

The Rate of mass gained by the rigid region must equal the rate mass lost by the plastic region. The mass balance is given by

$$\frac{dm}{dt} + \rho\delta\frac{dl}{dt} + \rho l\frac{d\delta}{dt} = 0 \quad (3.2)$$

The velocity of the material in the plastic region at the boundary has a velocity,

$$u = \varepsilon' l \quad (3.3)$$

For the body to be continuous, the velocity on the plastic side of the boundary must match that of the velocity of the rigid region and the velocity of the rigid region is that of the jet tip. Therefore,

$$u = \frac{dl}{dt} + \frac{d\xi}{dt} \quad (3.4)$$

Equations 3.3 and 3.4 are the constrains for kinematic compatibility and are analogous to the Stefan condition [4]. Solutions become ill-behaved when these conditions cannot be met when either rupture occurs or the jet becomes fully arrested.

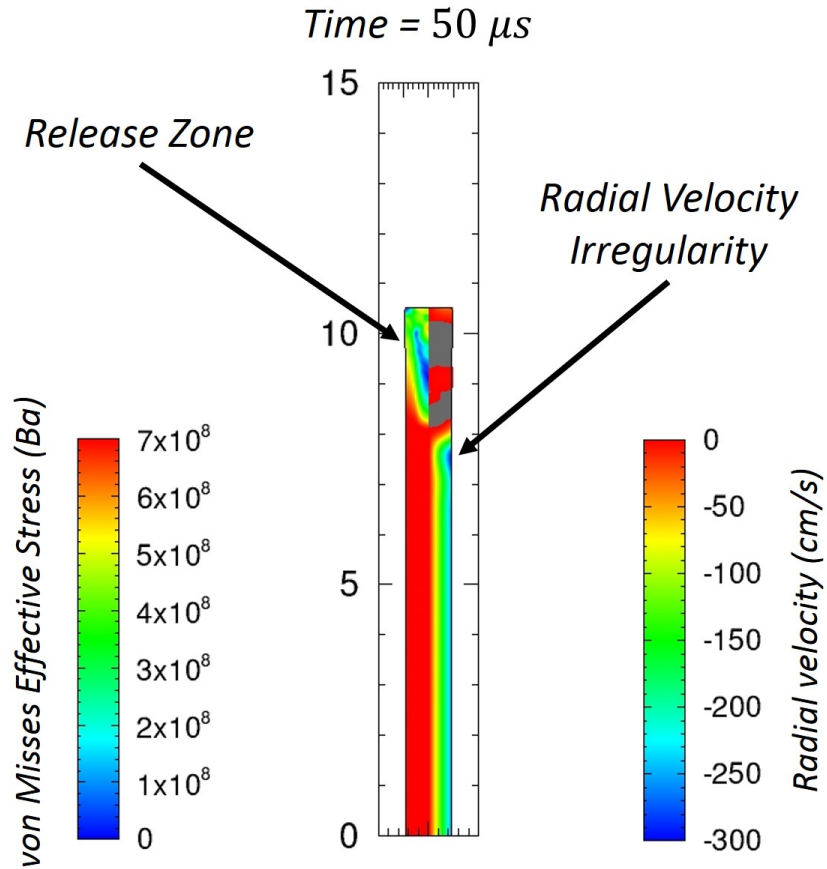


Figure 3.2: CTH simulation of the deformation arrest process with the radial velocity irregularity highlighted on the right. The left is the corresponding the von Misses effective stress profile.

Applying a momentum balance across the rigid-plastic interface results in Newton's second law for the variable mass rigid region as

$$-\sigma_Y \delta = m \frac{du}{dt} + \frac{dm}{dt} \Delta u$$

where Δu is the relative velocity between binding cross section segments. Due to the kinematic constraints, $\Delta u = 0$ resulting in equation 3.5.

$$-\sigma_Y \delta = m \frac{du}{dt} \tag{3.5}$$

Chapter 3. Reduced Order Modeling for Deformation Arrest

The rate of mechanical energy dissipated by thermoplastic heating is

$$\frac{dq}{dt} = \delta l \sigma_Y \dot{\varepsilon}'$$

Thermoelastic heating is negligible. The rate form of the energy balance for the system is

$$l^3 \varepsilon'^2 \frac{d\delta}{dt} + 2\delta l^3 \varepsilon' \frac{d\varepsilon'}{dt} + 3\delta l^2 \varepsilon'^2 \frac{dl}{dt} + 3u^2 \frac{dm}{dt} + 6mu \frac{du}{dt} + 6 \frac{dq}{dt} = 0 \quad (3.6)$$

The result is six equations for the six state variables, $\delta, l, \xi, \varepsilon', u,$ and m .

3.3.2 Dimensional Analysis

Dimensional analysis reveals self-similar behavior with behavior representing dimensionless groupings. To recast in dimensionless form, let

$$\begin{aligned} \xi &\equiv \frac{u_0}{\varepsilon'_0} Z \\ l &\equiv \frac{u_0}{\varepsilon'_0} L \\ \delta &\equiv \delta_0^2 D \\ u &\equiv u_0 U \\ \varepsilon' &\equiv \varepsilon'_0 E' \\ m &\equiv \rho \delta_0^2 \frac{u_0}{\varepsilon'_0} M \\ t &\equiv \frac{\delta_0}{u_0} \tau \end{aligned} \quad (3.7)$$

and for time derivatives, over-dot notation will be adopted, $\frac{d\bullet}{d\tau} \equiv \dot{\bullet}$. Substituting 3.7 into equations 1-6 reveals the dimensionless systems and two independent dimen-

sionless numbers and a third dimensionless combination.

$$\dot{M} = D\dot{Z} \quad (3.8a)$$

$$\dot{M} = -D\dot{L} - L\dot{D} \quad (3.8b)$$

$$U = \dot{E}L \quad (3.8c)$$

$$U = N_2(\dot{L} + \dot{Z}) \quad (3.8d)$$

$$-\frac{N_1}{N_2}D = M\dot{U} \quad (3.8e)$$

$$0 = \dot{E}^2 L^3 \dot{D} + 2D\dot{E}L^3 \ddot{E} + 3D\dot{E}^2 L^2 \dot{L} + 3U^2 \dot{M} + 6MU\dot{U} + 6\frac{N_1}{N_2}DL\dot{E} \quad (3.8f)$$

The dimensionless numbers N_1 and N_2 are

$$N_1 = \frac{\sigma_0}{\rho u_0^2}$$

$$N_2 = \frac{u_0}{\delta_0 \varepsilon'_0}$$

The square root of N_1 commonly appears in ductile jet stability analysis as the number of plastic velocity increment, $\frac{v_{pl}}{u_0}$. When the geometric quantity N_2 is included, $\frac{N_1}{N_2}$ is then a measure of the capacity to dissipate bulk internal kinetic energy gradients.

3.4 Analysis and Discussion

Approximate closed form solution to equations 3.8 results in theoretical rupture conditions, illustration of the velocity pullback phenomena as well as calculation of the instantaneous shape and position of the deformed body. By recognizing recurrence attributes in this system of DAE's, an asymptotic closed form solution can be obtained by an iterative substitution approach. Induction arguments are applied to guess the form of some of the system variables to obtain approximate solutions to other system variables. These solutions can then be inserted back into the system to

improve upon prior guesses or intermediate solutions. A direct numerical solution to the coupled system is obtained using the commercial solver Mathematica [61] that employs various differencing methods determined upon internal recognition of equation behaviors and numerical stability criterion. Intermediate closed form solutions and the numerical solution are compared to both CTH [17] and Abaqus [1] simulations until artificial boundary influences become significant to the overall behavior. The following initial conditions are applied during the solution process to equations 3.8,

$$M = 0$$

$$Z = 0$$

$$D = 1$$

$$L = 1$$

$$\dot{E} = 1$$

$$U = 1$$

3.4.1 Rupture Conditions

At early time, assume the rigid-plastic boundary propagates quickly relative to the change in jet dimensions or change in plastic strain-rate as noted by Walsh [91]. If D and \dot{E} are taken to behave like constants $D = 1$ and $\dot{E} = 1$, equations 3.8a, 3.8b, 3.8c, and 3.8e combined reduce to $\frac{N_1}{N_2} = Z\dot{Z}$ with solution 3.9 which is that of Kipp and Grady. Figure 3.3 compares equation 3.9 with the numerical solutions to equations 3.8 as well as the CTH and Abaqus simulation results for several different N_1 and N_2 before and after rupture.

$$Z = \sqrt{2\frac{N_1}{N_2}\tau} \tag{3.9}$$

Excellent agreement is obtained between FEA, finite-volume simulations, direct numerical and the closed form solutions 3.9. This illustrates that Z is relatively

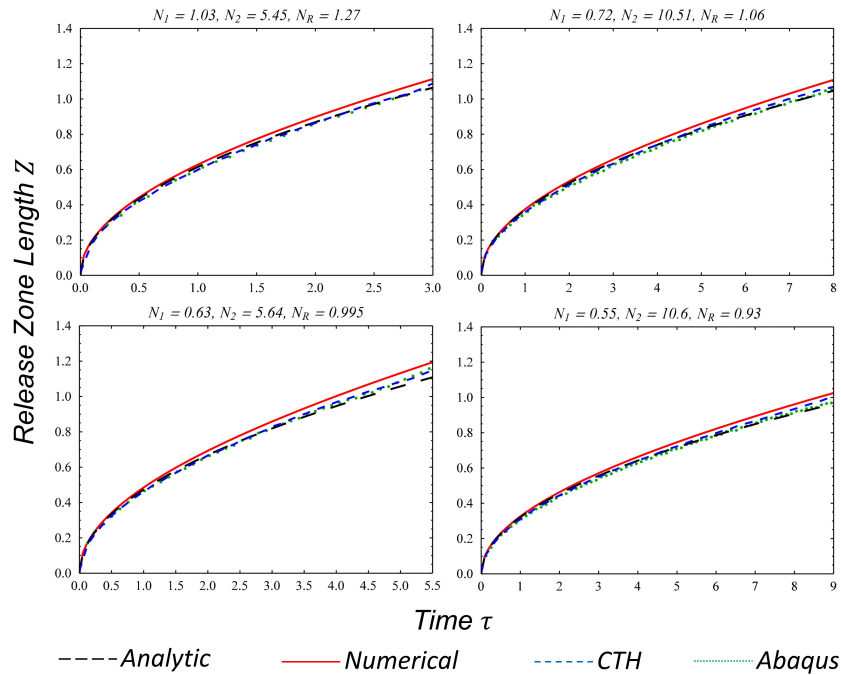


Figure 3.3: Dimensionless release zone length

insensitive to changes D and \dot{E} . Very close to the rupture condition shown on the bottom left of Figure 3.3, small deviation at late time suggests slightly more sensitivity to changes in D and \dot{E} on Z . With an explicit relation for Z , the thermodynamic equations in 3.8 are decoupled and an estimation for the plastic zone length can be obtained. By subtracting equation 3.8c from 3.8d and still allowing $\dot{E} = 1$ leads to the first order ODE for L ,

$$\dot{L} = \frac{1}{N_2}L - \dot{Z} \quad (3.10)$$

Using 3.9 to obtain \dot{Z} , the solution to 3.10 is

$$L = e^{\frac{\tau}{N_2}} \left[1 - \frac{\sqrt{2\pi N_1}}{2} \operatorname{erf} \left(\sqrt{\frac{\tau}{N_2}} \right) \right] \quad (3.11)$$

It is noted that N_2 acts as a process time constant by only appearing with τ . An improvement for D is now obtained. By eliminating \dot{M} between equation 3.8a and

3.8b results in the ODE to replace the initial assumption for D ,

$$L\dot{D} = -(\dot{L} + \dot{Z})D \quad (3.12)$$

By using both 3.9 and 3.11 to attain \dot{Z} and \dot{L} respectively, the solution for 3.12 is

$$D = e^{-\frac{\tau}{N_2}} \quad (3.13)$$

Further improvement for D will be made in the next section. Using equation 3.9 for \dot{Z} and substituting 3.11 into 3.8a or using 3.11 and 3.13 for L , \dot{L} , D , and \dot{D} into 3.8b results by integration for the release zone mass, given by

$$M = \frac{\sqrt{2\pi N_1}}{2} \operatorname{erf} \left(\sqrt{\frac{\tau}{N_2}} \right) \quad (3.14)$$

The rupture-number will be defined as $N_R \equiv \frac{\sqrt{2\pi N_1}}{2}$ which defines the rupture condition. For large τ , $\operatorname{erf} \left(\sqrt{\frac{\tau}{N_2}} \right)$ asymptotes to 1. If $N_R < 1$, the rupture number estimates the mass of the detached portion of the jet. If $\frac{\sqrt{2\pi N_1}}{2} > 1$, the jet becomes fully arrested without rupture. Equation 3.14 is shown with the numerical solution to equations 3.8 as well as the CTH and Abaqus simulation results in Figure 3.4 for several N_R before and after rupture. Although the closed form approximation slightly under-predicts at late time, the asymptotic behavior is in excellent agreement. Since the plastic velocity increment is an important measure for jet stability [33], the rupture condition is equivalently given by $\sqrt{\frac{\pi}{2}} \frac{V_{pl}}{u_0} < 1$. Note that this condition is directly the result of mass and momentum conservation with kinematic compatibility and rupture is only dependent on the yield strength and density for material properties and the initial conditions.

3.4.2 Velocity Pullback Phenomena

The system of equations 3.8 captures the velocity pullback phenomena and is exemplified by finding a solution for U . Since M looks like Z , using $M \approx Z$ in equation

Chapter 3. Reduced Order Modeling for Deformation Arrest

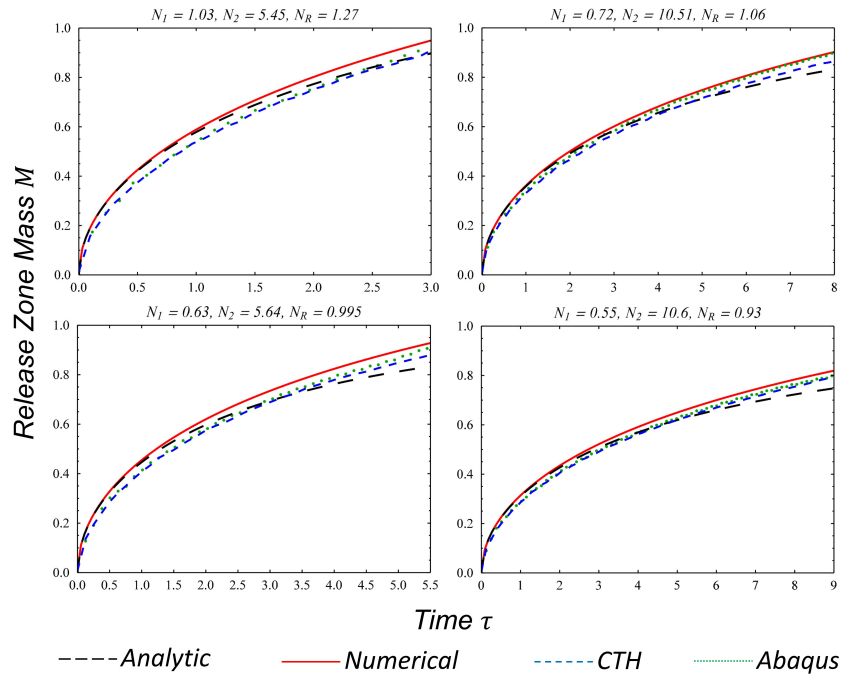


Figure 3.4: Dimensionless release zone mass

3.8e results in an ODE for U which is

$$-\frac{N_1}{N_2}D = Z\dot{U} \quad (3.15)$$

Taking D from 3.13 and Z from 3.9, a closed form solution of the resulting approximating ODE for U is

$$U = 1 - \frac{\sqrt{2\pi N_1}}{2} \operatorname{erf}\left(\sqrt{\frac{\tau}{N_2}}\right) \quad (3.16)$$

and is compared with the numerical solution, CTH and Abaqus simulations in Figure 3.5. Since slower moving material is joining the release zone that moves at a uniform velocity, the release zone velocity must decrease to conserve linear momentum. Deformation arrest happens gradually and non-uniformly within the body. As examined in the prior section, deviation at late time is a result of taking $M = Z$ which is a better assumption at early time when $D \approx 1$ however asymptotic

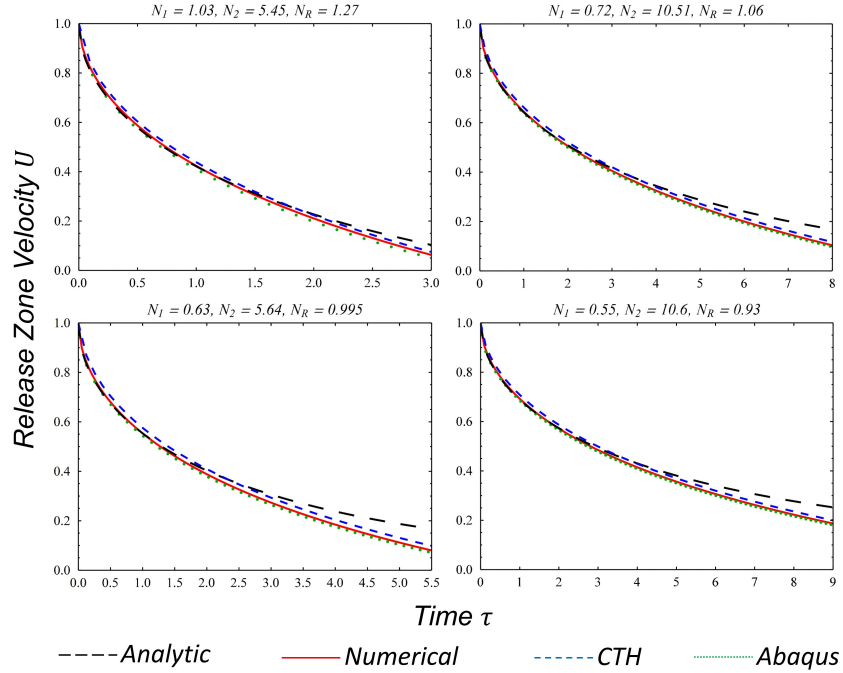


Figure 3.5: Velocity of the jet tip illustrating the velocity pullback phenomenon

behavior is in excellent agreement. If rupture occurs, the residual particle velocity is $U = 1 - N_R$. The strain rate is obtained in a straight forward manner from equation 3.8c and is given by

$$\dot{E} = e^{-\frac{\tau}{N_2}} \quad (3.17)$$

An improvement for D is achieved by eliminating \dot{M} between equations 3.8a and 3.8b and U between equations 3.8c and 3.8d. Then eliminating \dot{Z} between the combinations and recognizing that the solutions 3.17 and 3.13 are identical, the following ODE is obtained for D ,

$$\dot{D} = \frac{1}{N_2} D^2 \quad (3.18)$$

The solution is

$$D = \frac{N_2}{N_2 + \tau} \quad (3.19)$$

Chapter 3. Reduced Order Modeling for Deformation Arrest

Both the strain-rate and plastic region cross-section is found to be independent of material properties and varies only on time and the initial effective geometric ratio of the jet length to cross-section. Comparison of equation 3.17 and 3.19 with the numerical solutions to equations 3.8 as well as the CTH and Abaqus simulation results for several different N_1 and N_2 before and after rupture are shown in Figure 3.6 and Figure 3.7 respectively. Agreement is good for \dot{E} and excellent for D . The improvements for the closed form of D is necessary since D is sensitive to changes in \dot{E} . By observation, equation 3.19 is in excellent agreement with \dot{E} if $N_R \leq 1$.

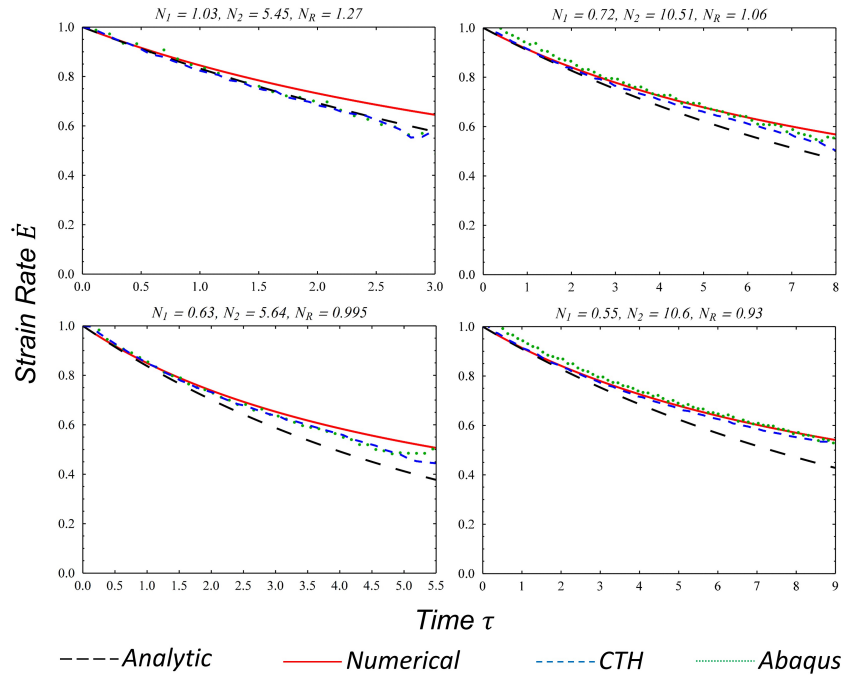


Figure 3.6: Dimensionless plastic zone strain rate

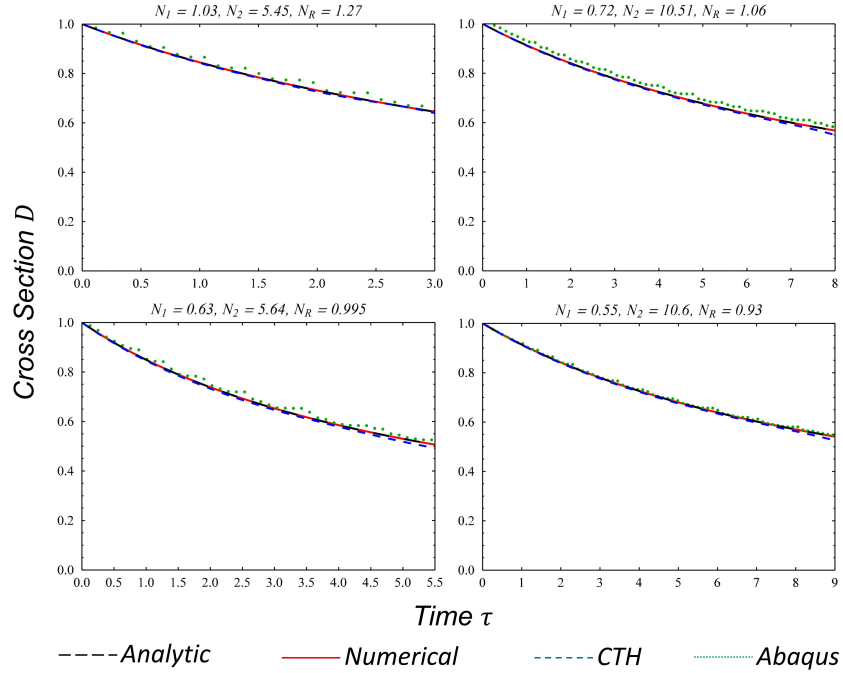


Figure 3.7: Dimensionless jet cross section

3.4.3 Rupture Strain

A better solution for the time profile in M can be obtained by recognizing from 3.16 that $U = 1 - M$. Therefore, from equation 3.8e, the ODE is

$$-\frac{N_1}{N_2}D = -M\dot{M} \quad (3.20)$$

using 3.19 for D , solution to 3.20 is

$$M = \sqrt{2N_1(\ln(N_2 + \tau) - \ln(N_2))} \quad (3.21)$$

If rupture does not occur, the time for deformation to cease is when equation 3.21 equals one or if rupture occurs $M = N_R$. Integrating equation 3.17 from $\tau = 0$ to the time in which deformation ceases gives the total plastic strain. The equation is

$$E = 1 - e^{\left(1 - e^{\frac{1}{2N_1}}\right)} \quad (3.22)$$

Chapter 3. Reduced Order Modeling for Deformation Arrest

If rupture occurs, integrating equation 3.19 and using $M = N_R$, the rupture strain is found to be

$$E_R = \frac{\pi}{4} \tag{3.23}$$

This result illustrates that the tensile rupture strain for a perfectly ductile material is approximately constant. An improvement for L is found by using 3.19 for D and \dot{D} and 3.21 for \dot{M} in equation 3.8b. The solution is

$$L = \frac{N_2 + \tau}{N_2} \left(1 - \sqrt{2N_1 (\ln(N_2 + \tau) - \ln(N_2))} \right) \tag{3.24}$$

Figure 3.8 compares equation 3.24 with the direct numerical solution of equations 3.8 as well as the CTH and Abaqus simulation results for several different N_1 and N_2 before and after rupture.

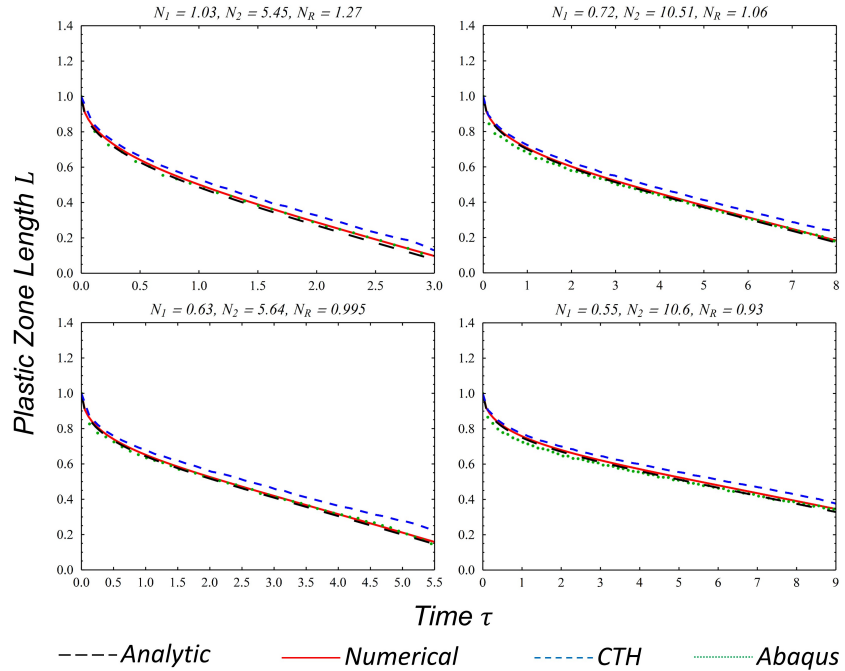


Figure 3.8: Dimensionless plastic zone length

3.4.4 Deformed Shape

The shape and position of the rigid region at any instant during deformation can be obtained by parametric representation. Using equations 4.14, 4.15 and 3.19, the outline of the jet tip at time τ is given by

$$\mathcal{R} = \frac{1}{2} \sqrt{\frac{N_2}{N_2 + s}} \quad (3.25a)$$

$$\mathcal{Z} = \frac{N_2 + \tau}{N_2} \left(1 - \sqrt{2N_1 (\ln(N_2 + \tau) - \ln(N_2))} \right) + \sqrt{2\frac{N_1}{N_2}\tau} - \sqrt{2\frac{N_1}{N_2}s} \quad (3.25b)$$

where the parameter s draws the contour for $0 \leq s \leq \tau$. The quantities \mathcal{R} and \mathcal{Z} are the dimensionless radial and axial coordinates respectively. Figure 3.9 shows the shape and position of an example jet tip that becomes fully arrested without rupture at several instances. The analytical and numerical solutions are shown together with CTH simulation results. Figure 3.10 is the same illustration instead for a jet that ruptures. Since the closed form for L overestimates at late time, the jet tip appears to travel slightly further. The body shape matches very closely in both figures.

3.5 Conclusions

An approach has been developed to predictively model the deformation arrest process for the inertially deforming ductile jet where strains can be very large and the body shape changes considerably. The solutions are shown to be in excellent agreement with FEA and shock-code simulation. The method employs continuum conservation laws with the propagation of a Mott-Lee release wave over a length where strain-rate and jet cross-section decreases drastically. Moving boundary analysis like those in Stefan-like problems is used to impose compatibility requirements for a continuous body through kinematic constraints. A finite jet body dissipates kinetic energy non-uniformly by internal plastic work. The time-varying plastic zone size is captured

Chapter 3. Reduced Order Modeling for Deformation Arrest

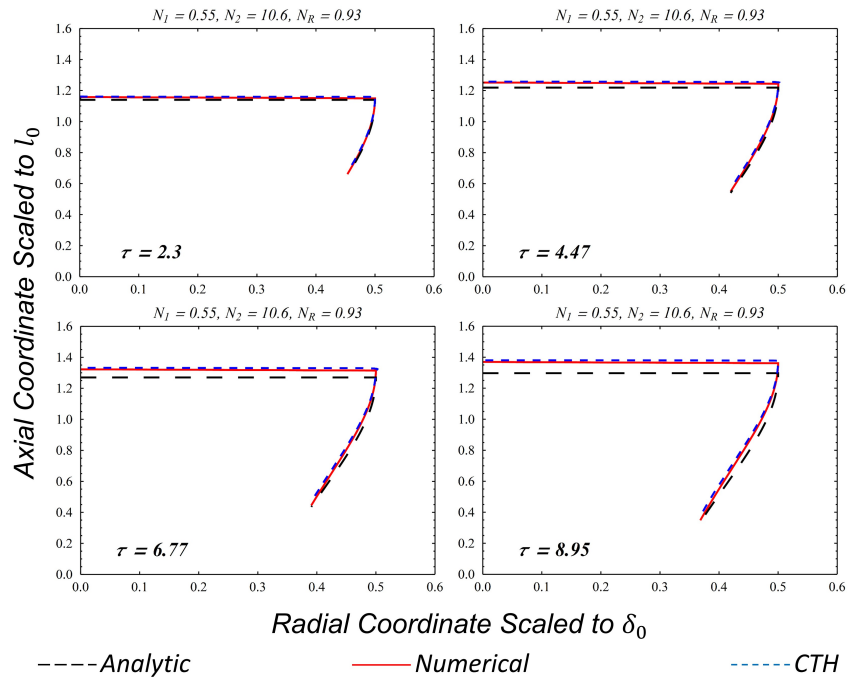


Figure 3.9: Release Zone contour during deformation arrest for a non-rupturing jet

with the strain-rate and cross-section shown to be independent of material properties. The velocity pullback phenomenon is demonstrated in solution.

The resulting system of differential-algebraic equations reveals key physical characteristics not yet before realized. Dimensional analysis uncovers two dimensionless numbers, one related to the plastic velocity increment common in plastic stability analysis and the other with the process time. The closed form solution process leads to theoretical rupture conditions, mass and velocity of the detached particle if rupture occurs, the time for motion to cease as well as the rupture strain. The shape and position of the body at any instant during deformation is obtained from the solution.

Solution of this system of equations is not limited to the initial and boundary conditions used here to illustrate the various phenomena discussed. Consideration of

Chapter 3. Reduced Order Modeling for Deformation Arrest

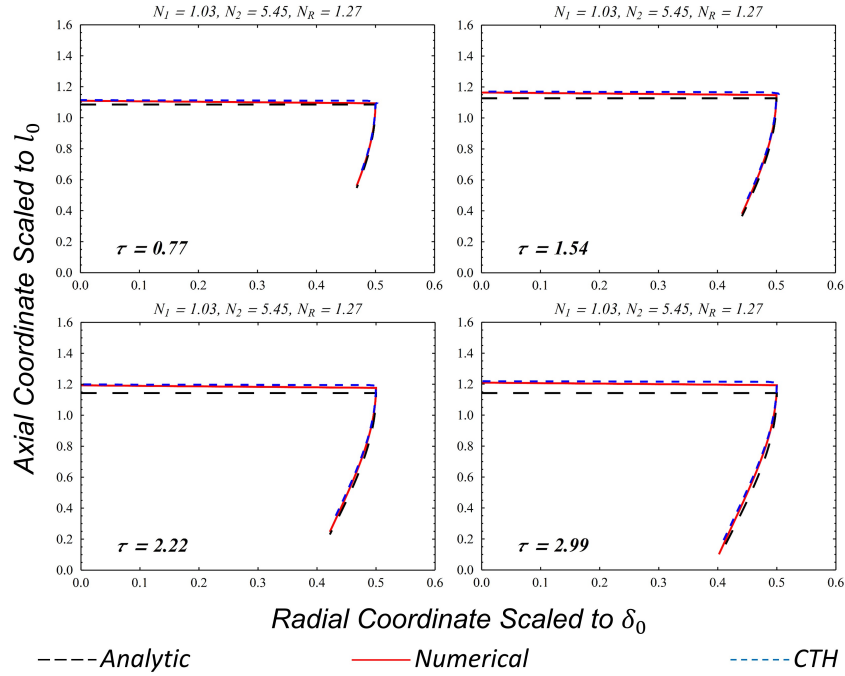


Figure 3.10: Release Zone contour during deformation arrest for a rupturing jet

this modeling approach may be adopted with appropriate modification to other problems in large-strain dynamic plasticity. Planned work consists of including viscoplastic material response to obtain a more material-general solution. Application of externally applied forces to the jet tip is to be included to show the relationship between loading and its impulse on rupture. Tensile rupture conditions may be obtained to the stretching of plastic hinges formed from transverse blast or impact loadings. This model can therefore be inserted into a multi-component structural model where necking and rupture is postulated to occur.

Chapter 4

Viscoplastic Effects on the Deformation Arrest Process

4.1 Abstract

It is shown that isotropic homogeneous constitutive equations for plastic flow-stress can be included in the governing system of equations for deformation arrest. This is exemplified using the Johnson-Cook viscoplastic relation [37] with the addition of a plastic work to temperature equation. The influence of thermal softening, strain-rate stiffening, and work hardening is discussed on the behavior of the inertially stretching jet.

4.2 Introduction

A mathematical theory for the deformation arrest process in large-strain dynamic plasticity has been proposed and exemplified in an inertially stretching jet. The

mathematical theory assumes idealized perfectly plastic material behavior. Real material effects important in the regime of strains and strain-rates where the theory is applied have been neglected in the development. These real material effects include thermal softening due to plastic-work heating, strain-rate stiffening, and work hardening.

Phenomenological and empirical viscoplastic constitutive relationships have been implemented in shock-codes and finite-element simulation tools for several decades with success in capturing these and other real material effects. One of the most common viscoplastic models for ductile materials is the Johnson-Cook flow stress equation [37]. It is given by

$$\sigma_y = (A + B\varepsilon^n) \left(1 + C \ln \left[\frac{\varepsilon'}{\varepsilon'_r} \right] \right) \left(1 - \left[\frac{T - T_0}{T_m - T_0} \right]^m \right) \quad (4.1)$$

where von-Mises yield stress is σ_y . The material specific constants A , B , C , n , and m are measured at the reference strain-rate ε'_r and temperature T_0 . The nominal yield stress is $\sigma_0 = A$. Plastic strain, strain-rate, temperature, and melting temperature are ε , ε' , T , and T_m respectively.

Viscoplastic influences are included in the deformation arrest theory by straightforward insertion of equation 4.1 and the addition of a plastic-work to temperature relationship. Some key consequences of these material effects on the inertially stretching jet illustrated in Figure 4.1 are highlighted.

The deformation arrest process for an inertially stretching jet with perfectly plastic flow stress is given by the system of differential algebraic equations (DAE's) in

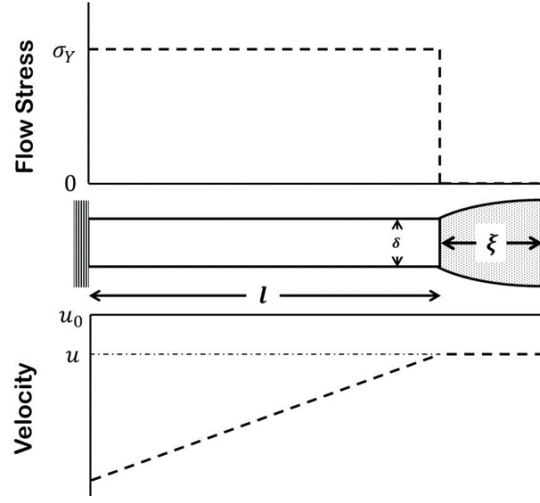


Figure 4.1: Inertially stretching jet illustration with representative flow stress and velocity profiles

4.2a through 4.2f.

$$\dot{M} = D\dot{Z} \quad (4.2a)$$

$$\dot{M} = -D\dot{L} - L\dot{D} \quad (4.2b)$$

$$U = \dot{E}L \quad (4.2c)$$

$$U = N_2(\dot{L} + \dot{Z}) \quad (4.2d)$$

$$-\frac{N_1}{N_2}D = M\dot{U} \quad (4.2e)$$

$$0 = \dot{E}^2 L^3 \dot{D} + 2D\dot{E}L^3 \ddot{E} + 3D\dot{E}^2 L^2 \dot{L} + 3U^2 \dot{M} + 6MU\dot{U} + 6\frac{N_1}{N_2}DL\dot{E} \quad (4.2f)$$

The dimensionless constants are defined by $N_1 \equiv \frac{\sigma_y}{\rho u_0^2}$ and $N_2 \equiv \frac{u_0}{\delta_0 \varepsilon'_0}$. The quantities σ_y , u_0 , δ_0 and ε'_0 are the nominal perfectly plastic yield stress, initial jet tip velocity, initial jet cross-section and the initial strain-rate respectively. The dimensionless variables in 4.2 are given to be $\xi \equiv \frac{u_0}{\varepsilon'_0} Z$, $l \equiv \frac{u_0}{\varepsilon'_0} L$, $\delta \equiv \delta_0^2 D$, $u \equiv u_0 U$, $\varepsilon' \equiv \varepsilon'_0 E'$, $m \equiv \rho \delta_0^2 \frac{u_0}{\varepsilon'_0} M$, and $t \equiv \frac{\delta_0}{u_0} \tau$ which are the release zone length, plastic zone length, plastic zone cross-section, jet tip velocity, plastic strain-rate, release zone mass, and

time respectively. The over-dot is used for the dimensionless time derivative. The closed-form solution process to equations 4.2 by an iterative substitution approach yield

$$Z = \sqrt{2\frac{N_1}{N_2}\tau} \quad (4.3a)$$

$$L = e^{\frac{\tau}{N_2}} \left[1 - \frac{\sqrt{2\pi N_1}}{2} \operatorname{erf} \left(\sqrt{\frac{\tau}{N_2}} \right) \right] \quad (4.3b)$$

$$M \approx \frac{\sqrt{2\pi N_1}}{2} \operatorname{erf} \left(\sqrt{\frac{\tau}{N_2}} \right) \quad (4.3c)$$

$$U = 1 - \frac{\sqrt{2\pi N_1}}{2} \operatorname{erf} \left(\sqrt{\frac{\tau}{N_2}} \right) \quad (4.3d)$$

$$D = \frac{N_2}{N_2 + \tau} \quad (4.3e)$$

$$\dot{E} = \begin{cases} e^{-\frac{\tau}{N_2}} & \text{if } \frac{\sqrt{2\pi N_1}}{2} > 1 \\ \frac{N_2}{N_2 + \tau} & \text{if } \frac{\sqrt{2\pi N_1}}{2} \leq 1 \end{cases} \quad (4.3f)$$

$$M = \sqrt{2N_2 (\ln(N_1 + \tau) - \ln(N_1))} \quad (4.3g)$$

$$\tau_{max} = N_2 \left(e^{\frac{N_R^2}{2N_1}} - 1 \right) \quad (4.3h)$$

$$E_{max} = \begin{cases} 1 - e^{\left(1 - e^{\frac{1}{2N_1}}\right)} & \text{if } \frac{\sqrt{2\pi N_1}}{2} > 1 \\ \frac{\pi}{4} & \text{if } \frac{\sqrt{2\pi N_1}}{2} \leq 1 \end{cases} \quad (4.3i)$$

The rupture number N_R is defined as

$$N_R \equiv \begin{cases} 1 & \text{if } \frac{\sqrt{2\pi N_1}}{2} > 1 \\ \frac{\sqrt{2\pi N_1}}{2} & \text{if } \frac{\sqrt{2\pi N_1}}{2} \leq 1 \end{cases}$$

4.3 Thermal Softening

Plastic zone heating due to internal plastic work reduces the flow stress acting on the release zone. Time scales are short enough ($\sim 10^{-3}$ sec) that heat conduction

is neglected and adiabatic conditions are presumed. Thermal softening behavior is isolated by zeroing the coefficients for strain-rate and strain hardening effects in simulation. Results show that thermal softening retards propagation of the rigid-plastic interface, decreasing the rate of mass gain in the no longer deforming portion of jet. The jet tip maintains a faster velocity, decreased cross section and longer plastic zone. Materials that readily soften reach reduced temperatures for the same strains. This is the result of decreasing material strength with increasing plastic work by means of temperature rise. As the material softens, the rate of temperature rise in the material is thereby reduced. In our simulations, the temperature rise in common engineering metals are of the order of tens of degrees C . This has negligible effect on the material strength, however perturbations in the plastic flow field grow more rapidly. Bulk thermal softening effects are apparent if the melt temperature is reduced to those of common plastics.

A temperature dependent functional form for the flow stress is added to the governing system of DAE's 4.2. The Johnson-Cook viscoplastic flow stress with only the thermal softening terms are used for illustration. The equation for flow stress is

$$\sigma_y = \sigma_0 \left(1 - \left[\frac{T - T_0}{T_m - T_0} \right]^m \right) \quad (4.4)$$

where σ_0 is the nominal quasi-static yield strength, T is the material temperature, T_m is the melting temperature, T_0 is the nominal reference temperature, and m is a fitted softening exponent that typically ranges between 0.3 and 1.8. For many common engineering metals, $m \approx 1$. Since the temperature rise is of the order of 10^0 to 10^1 degrees Kelvin, constant specific heat capacity c_T is assumed. The material temperature in the plastic zone is computed using

$$\rho c_T \frac{dT}{dt} = \beta \sigma_y \dot{\epsilon} \quad (4.5)$$

The right side of equation 4.5 is the rate of mechanical energy dissipated by plastic work per unit volume times the inelastic heat fraction β [22]. By scaling the flow

Chapter 4. Viscoplastic Effects on the Deformation Arrest Process

stress to the nominal yield strength and by means of distinguishing the homologous temperature while adopting the previously defined dimensionless scaling, equations 4.6 are added to the system 4.2.

$$Y = 1 - \Theta^m \quad (4.6a)$$

$$\dot{\Theta} = \frac{N_T}{N_2} Y \dot{E} \quad (4.6b)$$

A third dimensionless number, $N_T \equiv \frac{\beta\sigma_0}{\rho c_T(T_m - T_0)}$ appears in combination with N_2 . The quantity N_T is the fraction of temperature-available capacity for mechanical energy dissipation to that of the thermal energy gain required for melt. The quantity N_2 is a measure of arresting time scale. Generalization of equations 4.2e and 4.2f is needed to couple the variable yield strength. They become

$$-\frac{N_1}{N_2} Y D = M \dot{U} \quad (4.7a)$$

$$0 = \dot{E}^2 L^3 \dot{D} + 2D \dot{E} L^3 \ddot{E} + 3D \dot{E}^2 L^2 \dot{L} + 3U^2 \dot{M} + 6MU \dot{U} + 6 \frac{N_1}{N_2} Y \dot{E} D L \quad (4.7b)$$

Eliminating Y between equations 4.6a and 4.6b yields

$$\dot{\Theta} = \frac{N_T}{N_2} (1 - \Theta^m) \dot{E} \quad (4.8)$$

Substituting 4.3f for when $\frac{\sqrt{2\pi N_1}}{2} \leq 1$ and solving the resulting ODE for Θ , the consequences of N_T and m can be investigated. Closed-form solutions can be obtained for select m . If $m = 1$, the closed form solution for the temperature rise is

$$\Theta = 1 - \left(\frac{N_2}{N_2 + \tau} \right)^{N_T} \quad (4.9)$$

Equation 5.9 is in excellent agreement with CTH [17] simulation. The functional form illustrates that the temperature rises less rapidly with larger N_T . The influence of m is shown in Figure 4.2 by numerical integration. The quantity N_T is chosen for several common engineering metals. Smaller m decreases the rate of temperature rise.

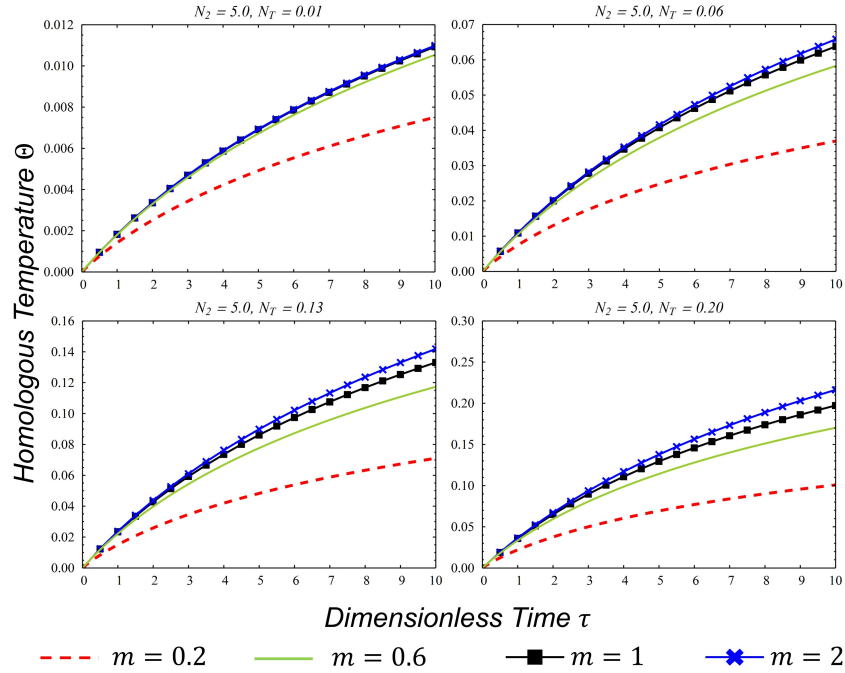


Figure 4.2: Influence of N_T and m on the homologous temperature as a function of time

Further illustrating that greater thermal softening decreases the rate of heating. In the same manner as demonstrated in chapter one for the body shape, the temperature profile along the jet can be obtained at any instant. This is shown in Figure 4.3.

The temperature of the plastic zone increases in time with increased strain. In the non-deforming zone, the jet tip is that of ambient temperature and rises along the jet axis towards the plastic zone. As the plastic interface propagates into the plastic zone, increasingly strained and heated material binds with the release zone creating what represents the history of the plastic zone thermal state. The approximate closed form for the temperature profile along the axis \mathcal{Z} coordinate at any instant τ is given by equations 4.10.

Chapter 4. Viscoplastic Effects on the Deformation Arrest Process

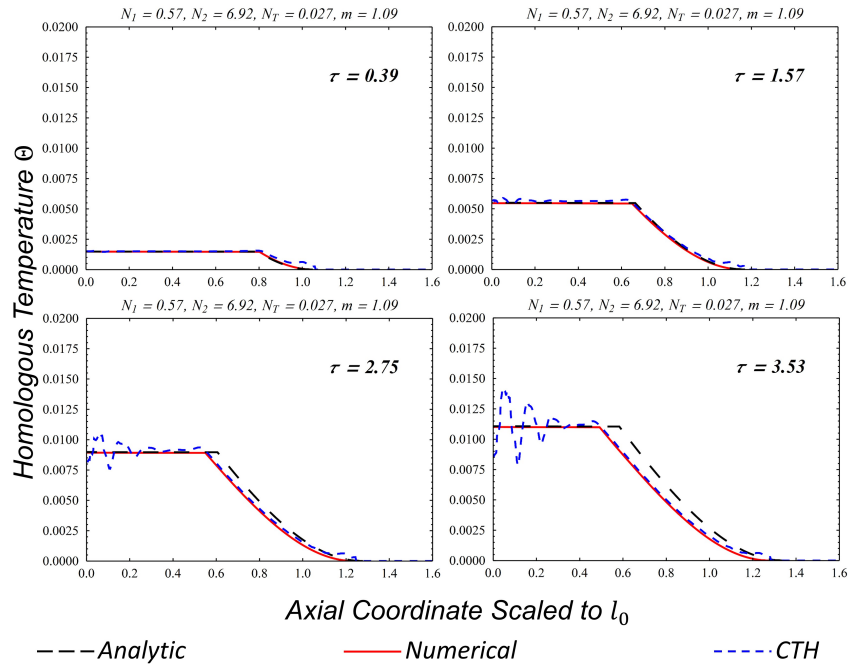


Figure 4.3: Homologous temperature profile along the jet length at several instances in time

$$\Theta = 1 - \left(\frac{N_2}{N_2 + s} \right)^{N_T} \quad (4.10a)$$

$$\mathcal{Z} = e^{\frac{\tau}{N_2}} \left[1 - \frac{\sqrt{2\pi N_1}}{2} \operatorname{erf} \left(\sqrt{\frac{\tau}{N_2}} \right) \right] + \sqrt{2 \frac{N_1}{N_2} \tau} - \sqrt{2 \frac{N_1}{N_2} s} \quad (4.10b)$$

The parameter s draws the contour for $0 \leq s \leq \tau$.

The late time oscillations in the plastic zone temperature during the CTH simulations are domain-boundary numerical artifacts enhanced by numerical instability induced from softening. When the oscillation front approaches the plastic boundary, these boundary influences begin to influence the bulk behavior of the jet and the simulations are then terminated. Figure 4.3 demonstrates that inclusion of equation 4.6 and 4.7 while using 4.3, thermal softening behavior on deformation arrest is incorporated without the inherent numerical challenges of shock-code simulation.

4.4 Strain-Rate Stiffening

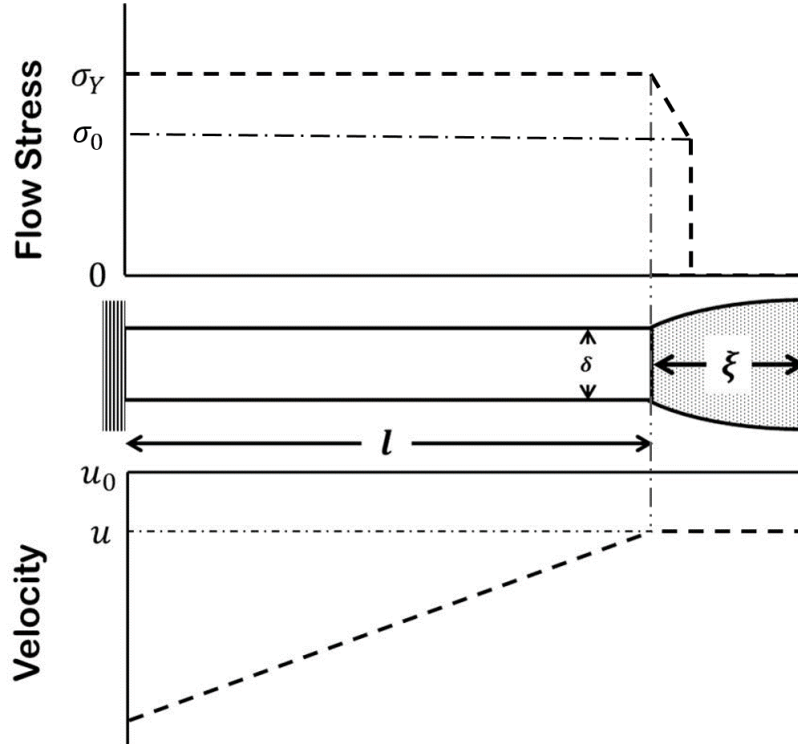


Figure 4.4: Inertially stretching jet illustration with representative flow stress and velocity profiles with strain-rate stiffening

During rapid loading, engineering metals can stiffen beyond nominal yield stress. If strain-rates increase during deformation, the material hardens while if strain-rates decrease, softening occurs instead. By isolating strain-rate dependence in simulation, it is observed that the distance from the root to the release boundary is no longer the plastic zone length. Instead, the release boundary leads the yielding interface in the plastic zone and is located where the inflections in yield state and material velocity correspond. This is illustrated schematically in Figure 4.4. Although the material between the release boundary and the elastic-plastic interface has a non-zero plastic strain-rate, the axial velocity is uniform with the entire release zone. The rigid-plastic boundary in equations 4.2 is placed at the yield state inflection coordinate

as opposed to the elastic-plastic interface. Equations 4.7 and 4.11 allow strain-rate effects to be captured. Isolating strain-rate stiffening, the Johnson-Cook flow stress is given by

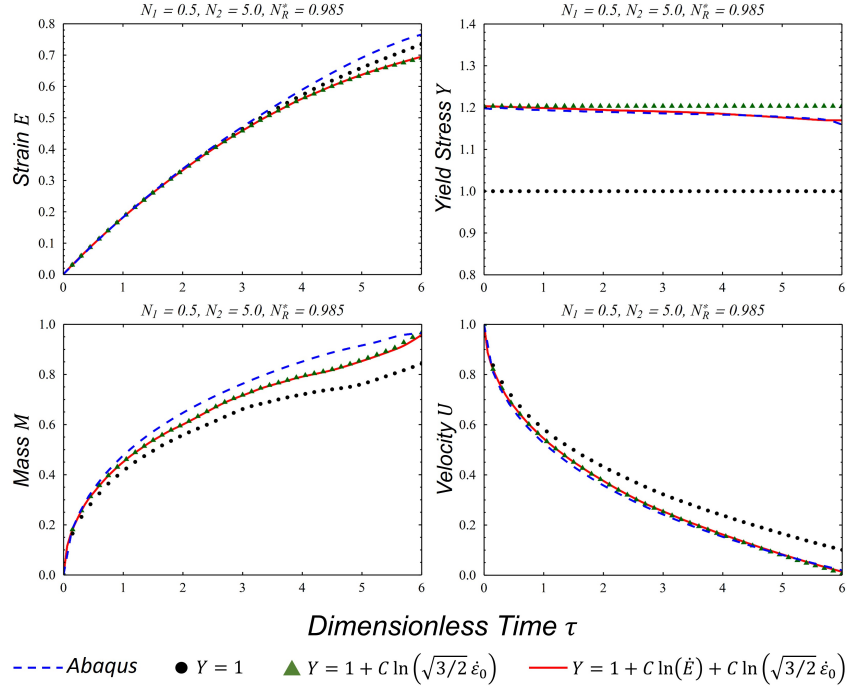


Figure 4.5: Comparison of Abaqus simulation with the numerical DAE solutions for strain-rate stiffening shown with the strain-rate shift and the perfectly plastic reference case where $Y = 1$

$$\sigma_y = \sigma_0 \left(1 + C \ln \left[\sqrt{\frac{3}{2}} \frac{\dot{\epsilon}'}{\dot{\epsilon}_r'} \right] \right) \quad (4.11)$$

The material constant C typically ranges between 6×10^{-3} to 6×10^{-2} and $\sqrt{\frac{3}{2}} \dot{\epsilon}'$ is the equivalent von-Mises deviatoric plastic strain-rate with $\dot{\epsilon}_r'$ as the reference strain-rate. In non-dimensional form, equation 4.12 becomes

$$Y = 1 + C \ln \left[\dot{E} \right] + C \ln \left[\sqrt{\frac{3}{2}} \frac{\dot{\epsilon}_0'}{\dot{\epsilon}_r'} \right] \quad (4.12)$$

The third term on the right-hand side is a time independent strain-rate shift in yield stress. Inserting equation 4.12 into the system 4.2 again with 4.7 closes the system. Solutions are in excellent agreement with Abaqus [1] simulation and is illustrated in Figure 4.5. For reference, the solutions for the perfectly plastic cases, $Y = 1$ and for $Y = 1 + C \ln \left[\sqrt{\frac{3}{2}} \frac{\dot{\varepsilon}'_0}{\dot{\varepsilon}'_r} \right]$ are shown. For typical values of C , the perfectly plastic solution with the time independent strain-rate shift is nearly indistinguishable from the full solution. The quantity N_R^* is defined as the rupture number using the strain-rate shifted yield stress. The offset between the numerical and Abaqus solutions for the mass is due to uncertainty in extracting the yielding stress inflection coordinate from simulation output. Using the same technique used to determine the temperature distribution, the total plastic strain distribution can be obtained.

4.5 Work Hardening

In simulation, total plastic strains reach order 10^{-1} to 10^0 . Since the strains are large, work hardening is significant and increases the flow stress by several times during deformation. Work hardening can significantly increase the initial jet tip velocity required for jet rupture. To illustrate this effect, the yield stress is given by Ludwik's equation[60]. Let

$$\sigma_y = \sigma_0 + B\varepsilon^n \quad (4.13)$$

be the flow stress where B is the hardening coefficient, m is the hardening exponent and ε the total plastic strain. To include in the system 4.2, the dimensionless form of equation 4.13 is

$$Y = 1 + \frac{B}{\sigma_0} E^n \quad (4.14)$$

The relationship between E and \dot{E} is

$$E = \frac{1}{N_2} \int_0^\tau \dot{E} d\tau \quad (4.15)$$

Chapter 4. Viscoplastic Effects on the Deformation Arrest Process

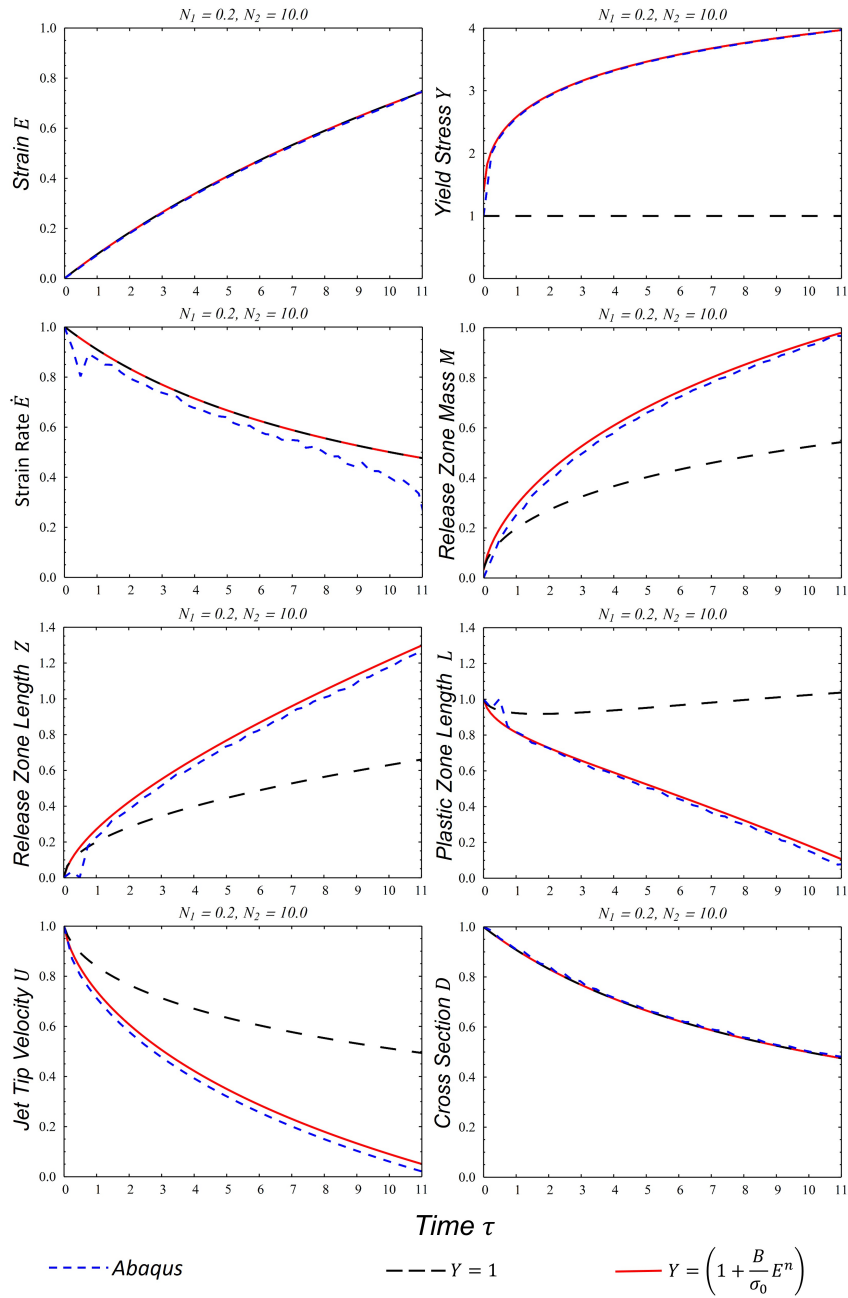


Figure 4.6: Comparison of Abaqus simulation with the numerical DAE solutions for work hardening shown with the perfectly plastic reference case where $Y = 1$

Figure 4.6 compares the solutions of E , Y , M and U with and without work hardening to Abaqus solutions for example N_1 and N_2 near rupture. During the deformation process, the yield strength increases by a factor of 4. This accelerates the growth of the release zone and enhances the velocity pullback. Greater mechanical energy is absorbed as plastic work and the time for motion to cease reduces. Note that the plastic strain, strain-rate, and plastic zone-cross section is independent of material properties. The systematic offset is a result of estimating the location of the plastic interface within the simulation due to the slight curvature in the interface. The strain-rate deviation at late time is due to large sensitivity in U and L as L becomes small.

4.6 Combined Effects

The three viscoplastic effects discussed are combined using the Johnson-Cook product description given by equation 4.1 [37]. In dimensionless form, the system of

Chapter 4. Viscoplastic Effects on the Deformation Arrest Process

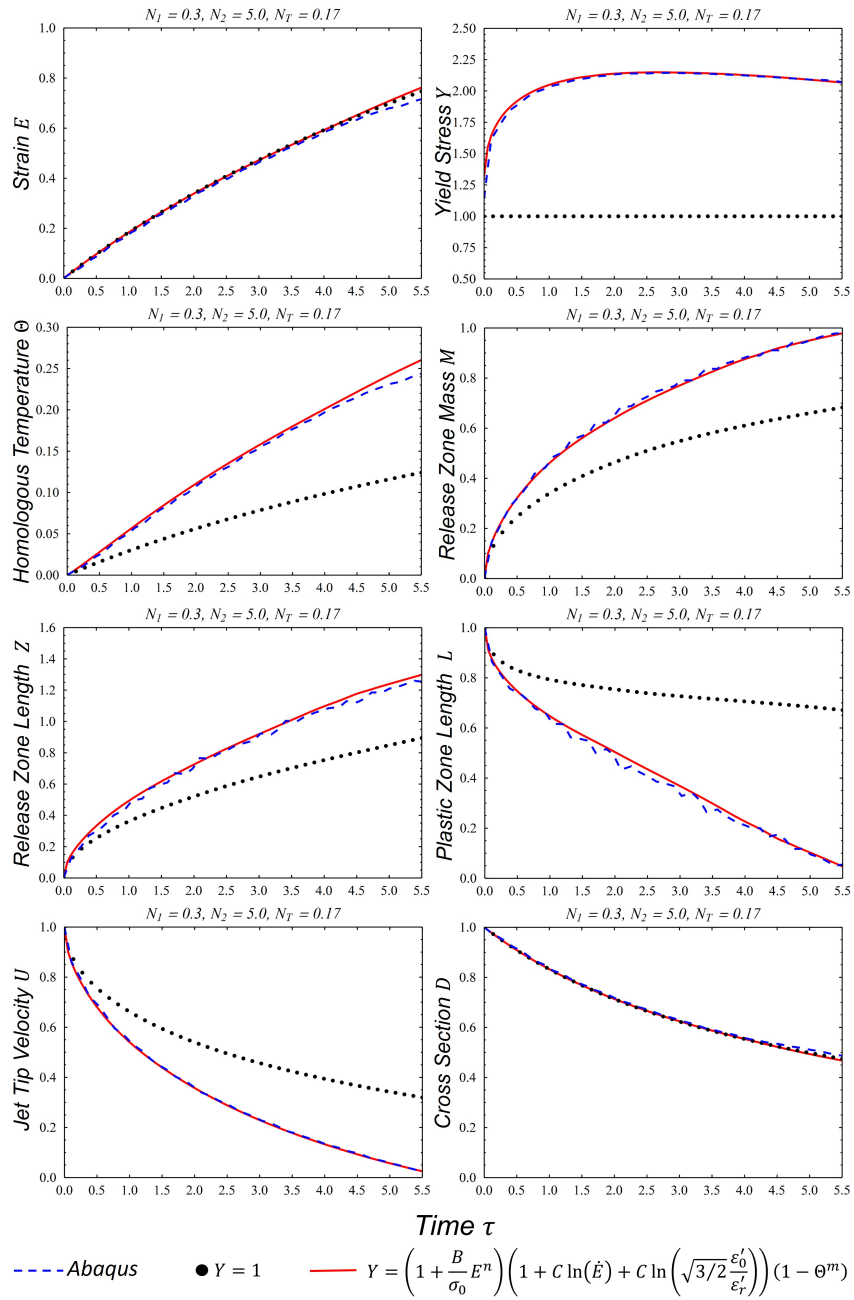


Figure 4.7: Comparison of Abaqus simulation with the numerical DAE solutions with combined viscoplastic effects shown with the perfectly plastic reference case where $Y = 1$

DAE's including the temperature equation and full Johnson-Cook equation is

$$\dot{M} = D\dot{Z} \quad (4.16a)$$

$$\dot{M} = -D\dot{L} - L\dot{D} \quad (4.16b)$$

$$U = \dot{E}L \quad (4.16c)$$

$$U = N_2(\dot{L} + \dot{Z}) \quad (4.16d)$$

$$-\frac{N_1}{N_2}YD = M\dot{U} \quad (4.16e)$$

$$\dot{\Theta} = \frac{N_T}{N_2}Y\dot{E} \quad (4.16f)$$

$$0 = \dot{E}^2 L^3 \dot{D} + 2D\dot{E}L^3\ddot{E} + 3D\dot{E}^2 L^2 \dot{L} + 3U^2 \dot{M} + 6MU\dot{U} + 6\frac{N_1}{N_2}YDL\dot{E} \quad (4.16g)$$

$$Y = \left(1 + \frac{B}{\sigma_0}E^n\right) \left(1 + C \ln \left[\dot{E}\right] + C \ln \left[\sqrt{\frac{3}{2}}\frac{\varepsilon'_0}{\varepsilon'_r}\right]\right) (1 - \Theta^m) \quad (4.16h)$$

Numerical solution to equation 4.16 match Abaqus simulations. Comparison is shown in Figure 4.7. For reference, the solution for $Y = 1$ is also shown. In this example, work hardening dominates early time by the quick rise in yield stress. Thermal softening becomes influential at late time due to the increased flow stress. Plastic strain increases monotonically and independent of material properties. Also, note that the jet cross-section is independent of material properties. The net effect due to viscoplasticity is a more rapid deformation arrest process.

4.7 Conclusions

Using the Johnson-Cook flow stress equation, viscoplastic effects on the deformation arrest process in an inertially stretching jet have been obtained. A temperature equation that relates internal plastic work to the homologous temperature is added to the governing system of differential algebraic equations. A dimensionless num-

ber, N_T that relates the conversion of mechanical energy to a temperature-available internal energy gain for melt appears representing the influence of thermal softening. It is shown that increased thermal softening reduces the rate of temperature rise and the temperature profile at any instant in time can be obtained. Strain-rate stiffening is shown to cause an upward shift in yield stress. Due to the logarithmic nature of the strain-rate in the Johnson-Cook equation, the flow-stress drop is minor during deformation. The uniform axial-velocity segment at the jet tip was found to extend into the plastic region. Since the strains are large and increase rapidly, work hardening has the most significant effect. A sharp rise in flow stress occurs followed by a significantly increased velocity pullback effect. When all the effects are combined, work-hardening is dominant and thermal softening effects may become apparent depending on N_T at late time.

Although this analysis implemented only the Johnson-Cook relationship, the approach illustrated is not restricted to this constrictive model. Other relationships that more accurately represent other isotropic homogeneous materials can be inserted instead. This study demonstrates general and robust attributes to the deformation arrest theory proposed prior.

Chapter 5

The Application of External and Coupling Loads on Deformation Arrest in Tensile Ductile Stretching

5.1 Abstract

External and coupling loads have been applied to the mathematical treatment proposed for deformation arrest in ductile stretching. Closed form solutions are obtained for the application of a tensile step loading on the jet tip. Analysis results in the rectangular-hyperbolic relationship between the loading and its impulse on the rupture threshold. The asymptote for minimum impulse at maximum loading is found to be dependent on both the jet slender ratio and the kinetic energy density to yield strength ratio. The asymptote for the minimum pressure at maximum loading is found to only depend on the kinetic energy density to yield strength ratio. Drag

resistance has been applied to the jet tip with little influence on jet motion unless the density of the surrounding fluid is comparable to the jet material.

Coupling the deformation arrest process for the linearly stretching ductile jet to a single-mode beam in phase 3 motion with angular deflection has been accomplished. The Zhao response number [111] appears in the dimensional analysis. Solution results show complicated features including rupture and full arrest. Other solutions show behaviors warranting further study.

5.2 Introduction

A method has been proposed to mathematically represent the deformation arrest process in an inertially stretching jet. In the problem formulation, the jet tip is stress-free and released suddenly to initiate the arrest process. However, problems of engineering interest require loadings to be applied to the jet tip. Generalizing the inertial jet deformation arrest problem to include external loads can lead to solution methods to current unsolved problems in engineering. In this chapter, such generalization is illustrated.

Loading-impulse relationships have been essential in the study of structural response to dynamic loadings and their engineering applications. Traditionally, the task is to reduce complexity by applying simplifying assumptions to a structure model for the deflections [29, 55, 56]. The results are mass-spring-damper like single degree-of-freedom (SDOF) systems. A time dependent loading is then applied and estimates on the final deflections are obtained as a function of loading magnitude and impulse. Defining deflection based damage criterion for SDOF systems representing structure failure is not well subscribed. However, it is recognized that load-impulse diagrams for a given deflection are of the rectangular-hyperbolic form with minimum load and minimum impulse asymptotes [2].

Practical calculations in structural dynamic plasticity are either performed as quasi-static or dynamic with impulsive-velocity initial conditions [39, 40, 79]. Spatial deflection profiles for elementary beams can be represented as a series of linked segments referred to as deformation modes. The motion of the segments upon loading occurs in 3 phases. The first phase is during the loading application where plastic hinges that resist rotational motion via the plastic moment M_p form at the root. If the boundary conditions are appropriate, plastic hinges also form at interior points and travel along the beam length as deflection progresses. In phase 2, the loading is removed and the motion of the interior hinges can change direction. In the final phase, the hinges become stationary and the beam segments rotate and translate as rigid bodies until motion ceases.

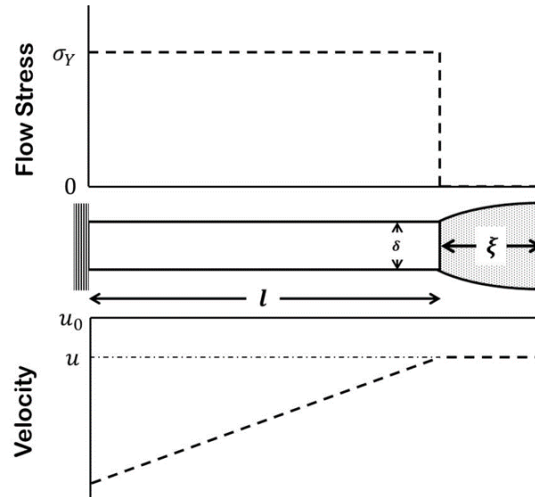


Figure 5.1: Inertially stretching jet illustration with representative flow stress and velocity profiles

When tensile stretching occurs as opposed to rotation about plastic hinges, the deformation arrest process in the viscoplastic inertially stretching jet shown in Figure 5.1 is applied. The mathematical representation is given by the system of differential

algebraic equations (DAE's) given by 5.1a through 5.1f

$$\dot{M} = D\dot{Z} \quad (5.1a)$$

$$\dot{M} = -D\dot{L} - L\dot{D} \quad (5.1b)$$

$$U = \dot{E}L \quad (5.1c)$$

$$U = N_2(\dot{L} + \dot{Z}) \quad (5.1d)$$

$$-\frac{N_1}{N_2}YD = M\dot{U} \quad (5.1e)$$

$$0 = \dot{E}^2L^3\dot{D} + 2D\dot{E}L^3\ddot{E} + 3D\dot{E}^2L^2\dot{L} + 3U^2\dot{M} + 6MU\dot{U} + 6\frac{N_1}{N_2}YDL\dot{E} \quad (5.1f)$$

The variable Y represents the viscoplastic relationship. The dimensionless constants are defined by $N_1 \equiv \frac{\sigma_0}{\rho u_0^2}$ and $N_2 \equiv \frac{u_0}{\delta_0 \varepsilon'_0}$. The quantities σ_0 , u_0 , δ_0 and ε'_0 are the nominal yield stress, initial jet tip velocity, initial jet cross-section and the initial strain-rate respectively. The dimensionless variables in 4.2 are given to be $\xi \equiv \frac{u_0}{\varepsilon'_0}Z$, $l \equiv \frac{u_0}{\varepsilon'_0}L$, $\delta \equiv \delta_0^2 D$, $u \equiv u_0 U$, $\varepsilon' \equiv \varepsilon'_0 E'$, $m \equiv \rho \delta_0^2 \frac{u_0}{\varepsilon'_0} M$, and $t \equiv \frac{\delta_0}{u_0} \tau$ which are the release zone length, plastic zone length, plastic zone cross-section, jet tip velocity, plastic strain-rate, release zone mass, and time respectively. The over-dot is used for the dimensionless time derivative. For a perfectly-plastic $Y = 1$ material, the closed-form solution process to equations 5.1 by an iterative substitution approach

yield

$$Z = \sqrt{2\frac{N_1}{N_2}\tau} \quad (5.2a)$$

$$L = e^{\frac{\tau}{N_2}} \left[1 - \frac{\sqrt{2\pi N_1}}{2} \operatorname{erf} \left(\sqrt{\frac{\tau}{N_2}} \right) \right] \quad (5.2b)$$

$$M \approx \frac{\sqrt{2\pi N_1}}{2} \operatorname{erf} \left(\sqrt{\frac{\tau}{N_2}} \right) \quad (5.2c)$$

$$U = 1 - \frac{\sqrt{2\pi N_1}}{2} \operatorname{erf} \left(\sqrt{\frac{\tau}{N_2}} \right) \quad (5.2d)$$

$$D = \frac{N_2}{N_2 + \tau} \quad (5.2e)$$

$$\dot{E} = \begin{cases} e^{-\frac{\tau}{N_2}} & \text{if } \frac{\sqrt{2\pi N_1}}{2} > 1 \\ \frac{N_2}{N_2 + \tau} & \text{if } \frac{\sqrt{2\pi N_1}}{2} \leq 1 \end{cases} \quad (5.2f)$$

$$M = \sqrt{2N_2 (\ln(N_1 + \tau) - \ln(N_1))} \quad (5.2g)$$

$$\tau_{max} = N_2 \left(e^{\frac{N_R^2}{2N_1}} - 1 \right) \quad (5.2h)$$

$$E_{max} = \begin{cases} 1 - e^{\left(1 - e^{\frac{1}{2N_1}}\right)} & \text{if } \frac{\sqrt{2\pi N_1}}{2} > 1 \\ \frac{\pi}{4} & \text{if } \frac{\sqrt{2\pi N_1}}{2} \leq 1 \end{cases} \quad (5.2i)$$

The rupture number N_R is defined as

$$N_R \equiv \begin{cases} 1 & \text{if } \frac{\sqrt{2\pi N_1}}{2} > 1 \\ \frac{\sqrt{2\pi N_1}}{2} & \text{if } \frac{\sqrt{2\pi N_1}}{2} \leq 1 \end{cases}$$

5.3 Loading of the Tensile Jet

The influence of an externally applied loading on the deformation arrest process is investigated by applying a force to the jet tip as illustrated in Figure 5.2. The force can be an explicit function of time, a function of any of the system variables or a coupling action to some-other mechanical system. An example of each will be illustrated.

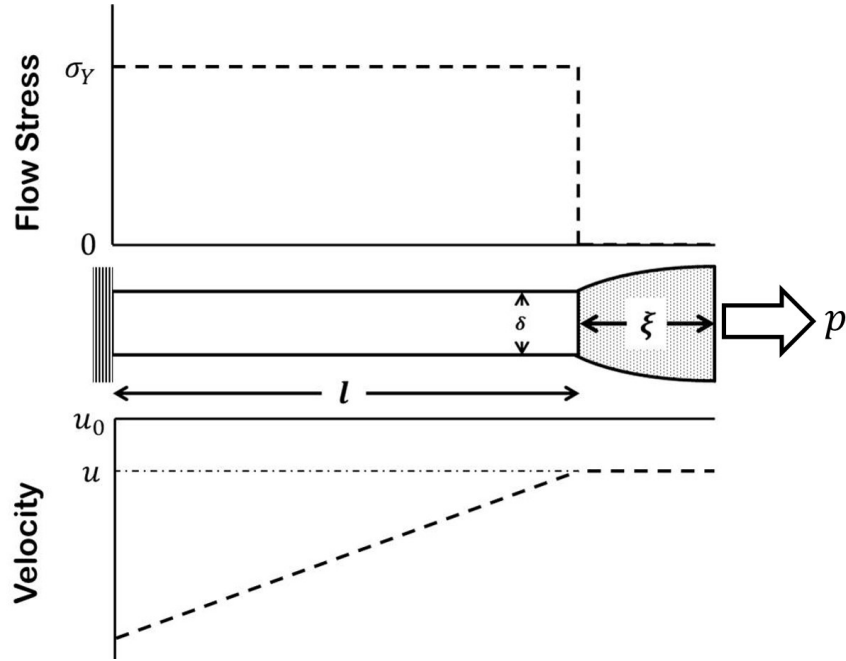


Figure 5.2: Inertially stretching jet illustration with representative flow stress and velocity profiles with a tensile load

To formulate the most general case, let p be the applied force at the jet tip. The force-momentum balance is

$$p - \sigma_y \delta = m \frac{du}{dt} \quad (5.3)$$

The loading p adds or removes energy by mechanical work. The rate of mechanical work is pu . The energy conservation equation therefore becomes

$$l^3 \varepsilon'^2 \frac{d\delta}{dt} + 2\delta l^3 \varepsilon' \frac{d\varepsilon'}{dt} + 3\delta l^2 \varepsilon'^2 \frac{dl}{dt} + 3u^2 \frac{dm}{dt} + 6mu \frac{du}{dt} + 6\delta l \sigma_Y \varepsilon' - 6pu = 0 \quad (5.4)$$

By defining $p \equiv \sigma_0 \delta_0 P$, the dimensionless form of equation 5.3 is

$$\frac{N_1}{N_2} (P - YD) = M\dot{U} \quad (5.5)$$

and for 5.4,

$$\dot{E}^2 L^3 \dot{D} + 2D\dot{E}L^3 \ddot{E} + 3D\dot{E}^2 L^2 \dot{L} + 3U^2 \dot{M} + 6MU\dot{U} + 6\frac{N_1}{N_2} (Y\dot{E}DL - PU) = 0 \quad (5.6)$$

For positive P , the jet tip is being pulled and for negative P , pushing resistance is applied instead. In the next section, a step-loading pulling force is applied. The following section considers a pushing force by fluid drag. Lastly, a rigid beam with plastic hinges at the mid-point and root is coupled such that stretching at the beam attachment points can be represented.

5.3.1 Step Impulse and the P-I Diagram

Application of a pulling action on the jet tip is examined. Suppose the force p is $p = p_0(1 - H(t - t_1))$ where $H(t - t_1)$ is the unit step function and t_1 is the length of time for which p is applied. The impulse of p is $\iota_p = p_0 t_1$. The dimensionless form for p is

$$P = P_1(1 - H(\tau - \tau_1)) \quad (5.7)$$

The constant P_1 is defined by $P_1 \equiv \frac{p_0}{\sigma_0 \delta_0}$. The dimensionless impulse is $I_1 = P_1 \tau_1$. For simplicity, perfectly plastic material representation will be used. The resulting system of DAE's become

$$\dot{M} = D\dot{Z} \quad (5.8a)$$

$$\dot{M} = -D\dot{L} - L\dot{D} \quad (5.8b)$$

$$U = \dot{E}L \quad (5.8c)$$

$$U = N_2(\dot{L} + \dot{Z}) \quad (5.8d)$$

$$M\dot{U} = \frac{N_1}{N_2}(P - YD) \quad (5.8e)$$

$$0 = \dot{E}^2 L^3 \dot{D} + 2D\dot{E}L^3 \ddot{E} + 3D\dot{E}^2 L^2 \dot{L} + 3U^2 \dot{M} \\ + 6MU\dot{U} + 6\frac{N_1}{N_2}(Y\dot{E}DL - PU) \quad (5.8f)$$

$$P = P_1(1 - H(\tau - \tau_1)) \quad (5.8g)$$

Solution is now realized.

5.3.2 Closed Form Solution

The iterative substitution approach is used to find a closed form piecewise solution. First the solution for $\tau \leq \tau_1$ is obtained and then the solutions at τ_1 are used as initial conditions. The system is solved again for $\tau > \tau_1$.

Step Loading for When $\tau \leq \tau_1$

At early time, $D = 1$ and $\dot{E} = 1$ is assumed. The system of equations 5.8 then reduces to an ODE for Z . The solution is

$$Z = \sqrt{2\frac{N_1}{N_2}(1 - P_1)\tau} \quad (5.9)$$

Maintaining the assertion that $\dot{E} = 1$ and with the solution for Z , algebraic reduction results in an ODE for L for which

$$L = e^{\frac{\tau}{N_2}} \left[1 - \frac{\sqrt{2\pi N_1(1 - P_1)}}{2} \operatorname{erf} \left(\sqrt{\frac{\tau}{N_2}} \right) \right] \quad (5.10)$$

The loading has no effect on the jet cross-section. Therefore, for the first iteration D is taken to be

$$D = e^{-\frac{\tau}{N_2}} \quad (5.11)$$

With equation 5.15 and 5.9, integration of equation 5.8a yields the release zone mass,

$$M = \frac{\sqrt{2\pi N_1(1 - P_1)}}{2} \operatorname{erf} \left(\sqrt{\frac{\tau}{N_2}} \right) \quad (5.12)$$

By assuming $M \approx Z$ in equation 5.8e, the jet tip velocity is

$$U = 1 + \frac{P_1 \sqrt{\frac{2N_1(1 - P_1)\tau}{N_2}}}{1 - P_1} - \frac{\sqrt{2\pi N_1(1 - P_1)}}{2(1 - P_1)} \operatorname{erf} \left(\sqrt{\frac{\tau}{N_2}} \right) \quad (5.13)$$

A better solution for D is

$$D = \frac{N_2}{N_2 + \tau} \quad (5.14)$$

and \dot{E} is also independent of the loading. Therefore

$$\dot{E} = \frac{N_2}{N_2 + \tau} \quad (5.15)$$

Step Loading for When $\tau > \tau_1$

When the loading is release at $\tau = \tau_1$, in terms of P_1 and N_1 the system state is

$$Z_1 = \sqrt{2 \frac{N_1}{N_2} \left(\frac{I_1}{P_1} - I_1 \right)} \quad (5.16a)$$

$$L_1 = e^{\frac{I_1}{P_1 N_2}} \left[1 - \frac{\sqrt{2\pi N_1(1-P_1)}}{2} \operatorname{erf} \left(\sqrt{\frac{I_1}{P_1 N_2}} \right) \right] \quad (5.16b)$$

$$D_1 = e^{-\frac{I_1}{P_1 N_2}} \quad (5.16c)$$

$$M_1 = \frac{\sqrt{2\pi N_1(1-P_1)}}{2} \operatorname{erf} \left(\sqrt{\frac{I_1}{P_1 N_2}} \right) \quad (5.16d)$$

$$U_1 = 1 + \frac{P_1 \sqrt{\frac{2N_1 I_1 (1-P_1)}{P_1 N_2}}}{1-P_1} - \frac{\sqrt{2\pi N_1(1-P_1)}}{2(1-P_1)} \operatorname{erf} \left(\sqrt{\frac{I_1}{P_1 N_2}} \right) \quad (5.16e)$$

Equation 5.8 is solved again using equations 4.15 for initial conditions and integrating in time with respects to the shifted time $\zeta \equiv \tau - \tau_1 = \tau - \frac{I_1}{P_1}$. The solutions are

found to be

$$Z = \sqrt{2 \frac{N_1}{N_2} (\tau - I_1)} \quad (5.17a)$$

$$L = e^{\frac{\tau}{N_2}} \left[1 - \frac{\sqrt{2\pi N_1(1-P_1)}}{2} \operatorname{erf} \left(\sqrt{\frac{I_1}{P_1 N_2}} \right) \right] + e^{\frac{\tau - I_1}{N_2}} \frac{\sqrt{2\pi N_1}}{2} \left[\operatorname{erf} \left(\sqrt{\frac{I_1}{P_1 N_2} - \frac{I_1}{N_2}} \right) - \operatorname{erf} \left(\sqrt{\frac{\tau - I_1}{N_2}} \right) \right] \quad (5.17b)$$

$$M = \frac{\sqrt{2\pi N_1(1-P_1)}}{2} \operatorname{erf} \left(\sqrt{\frac{I_1}{P_1 N_2}} \right) - e^{\frac{-I_1}{N_2}} \frac{\sqrt{2\pi N_1}}{2} \left[\operatorname{erf} \left(\sqrt{\frac{I_1}{P_1 N_2} - \frac{I_1}{N_2}} \right) - \operatorname{erf} \left(\sqrt{\frac{\tau - I_1}{N_2}} \right) \right] \quad (5.17c)$$

$$U = 1 + \sqrt{2 \frac{N_1 P_1 I_1}{N_2(1-P_1)}} - \frac{1}{2} \sqrt{\frac{2\pi N_1}{1-P_1}} \operatorname{erf} \left(\sqrt{\frac{I_1}{P_1 N_2}} \right) + e^{\frac{-I_1}{N_2}} \frac{\sqrt{2\pi N_1}}{2} \left[\operatorname{erf} \left(\sqrt{\frac{I_1}{P_1 N_2} - \frac{I_1}{N_2}} \right) - \operatorname{erf} \left(\sqrt{\frac{\tau - I_1}{N_2}} \right) \right] \quad (5.17d)$$

$$D = \frac{N_2}{N_2 + \tau} \quad (5.17e)$$

$$\dot{E} = \frac{N_2}{N_2 + \tau} \quad (5.17f)$$

The numerical solution to equation 5.8 is shown with the closed form solution and Abaqus simulation in Figure 5.3. For reference, a no-loading solution for the same N_1 and N_2 is also shown. The loading is applied from $\tau = 0$ to $\tau = 0.5$. The growth of the release zone is reduced while the plastic zone length and jet tip velocity do not decrease significantly. When the load is released, a sudden change is seen in the jet behavior. The release zone grows rapidly and the jet velocity drops quickly.

The relationship between the loading magnitude P_1 and its impulse I_1 on the rupture threshold is obtained by finding P_1 corresponding to an I_1 in equation 5.17c at rupture. Deformation ceases when $U = 0$ giving $\tau = \tau_{max}$ which is substituted into equation 5.17c. The minimum P_1 for a value of I_1 for which $M < 1$ is then obtained by numerical inversion. The P-I diagram for several N_1 is shown in Figure 5.4 for

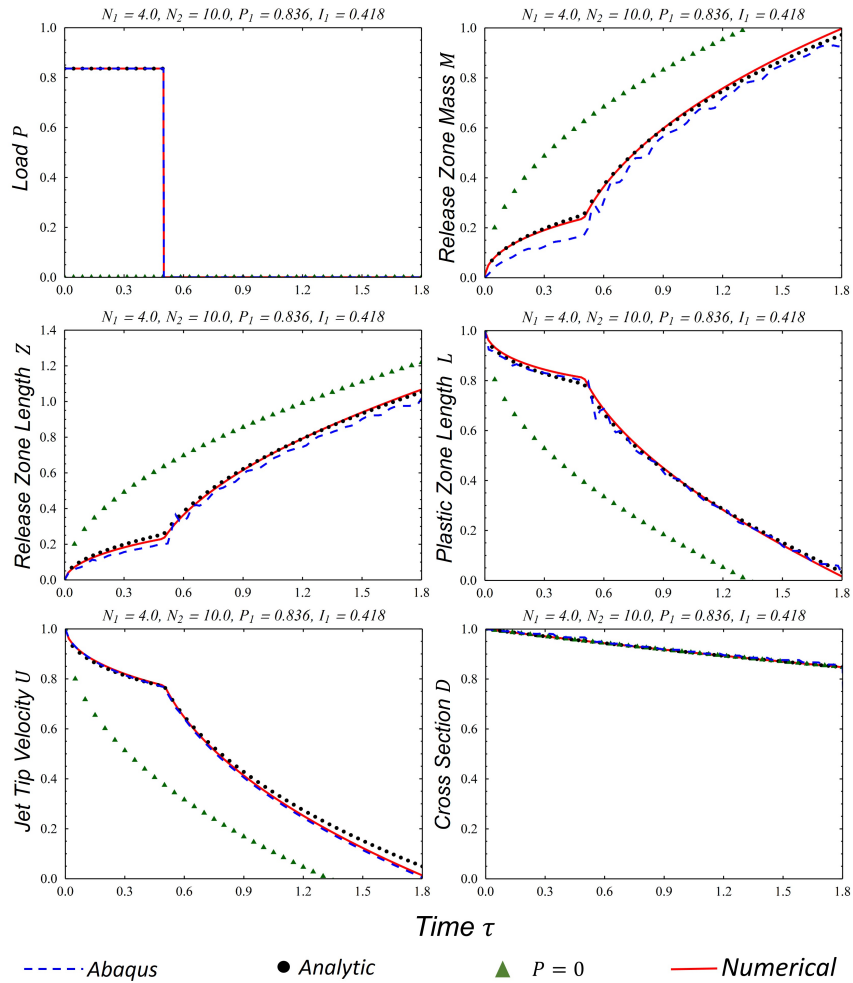


Figure 5.3: Solution comparison of the ductile jet with a tensile step loading

select values of N_2 . The rectangular-hyperbolic shape familiar to P-I diagrams for transverse beam loads is also shown to be case for the stretching jet. The asymptotic behaviors for minimum I_1 and P_1 are also observed. The minimum impulse required to cause rupture is the intersection of the P-I contour with the $P_1 = 1$ horizontal. The minimum impulse is found to be

$$I_{1,min} = -N_2 \ln \left(\frac{2}{\sqrt{2\pi N_1}} \right) \quad (5.18)$$

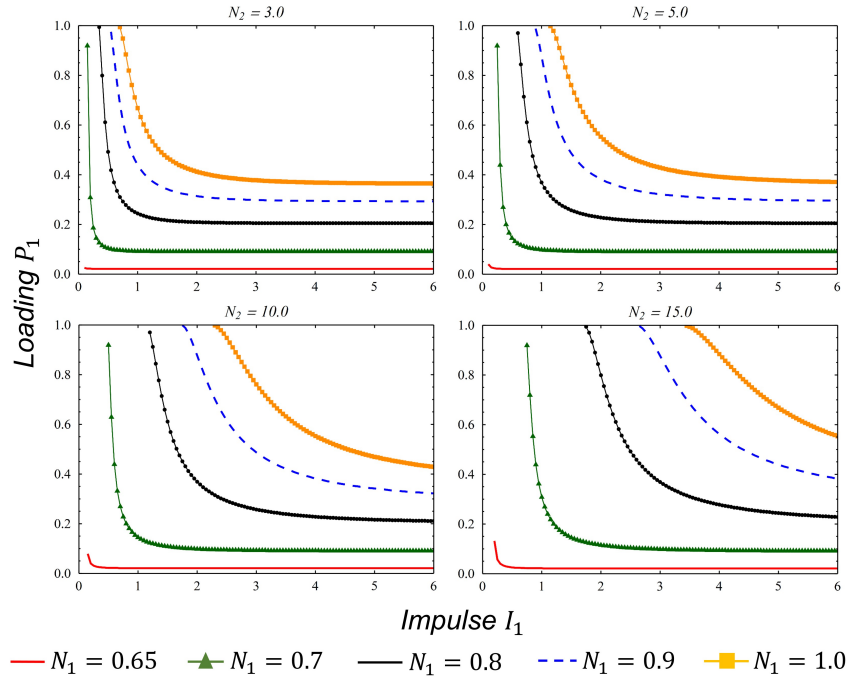


Figure 5.4: P-I relationship for a step impulse on the rupture threshold

The minimum P_1 required for rupture is the I_1 asymptote and is given by

$$P_{1,min} = 1 - \frac{2}{N_1\pi} \quad (5.19)$$

Note that the minimum impulse depends on both N_1 and N_2 while the minimum loading only depends on N_1 . For N_1 near the zero-load rupture condition $N_1 = \frac{2}{\pi}$, little loading is required regardless of impulse. For large N_1 , both the minimum impulse and the minimum loading must be larger.

5.4 Drag Resistance During Jet Motion

Consider drag resistance applied to the jet tip with perfectly plastic material. For simplicity, assume the drag force is given by $p = -\frac{1}{2}\rho_{fluid}\delta_0 u^2$. In dimensionless

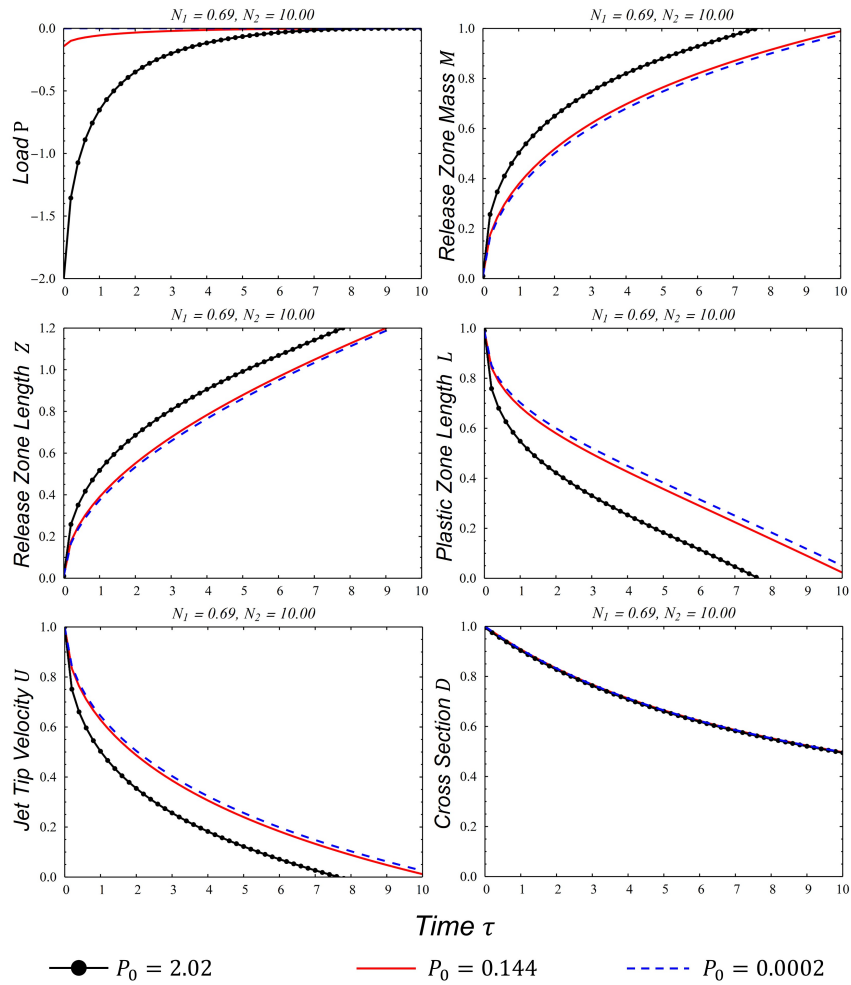


Figure 5.5: Solution of the inertial jet with drag resistance

form,

$$P = -P_0 U^2 \tag{5.20}$$

where $P_0 = \frac{\rho_{fluid} u_0^2}{2\sigma_y}$. The governing system of equations are now

$$\dot{M} = D\dot{Z} \quad (5.21a)$$

$$\dot{M} = -D\dot{L} - L\dot{D} \quad (5.21b)$$

$$U = \dot{E}L \quad (5.21c)$$

$$U = N_2(\dot{L} + \dot{Z}) \quad (5.21d)$$

$$M\dot{U} = \frac{N_1}{N_2}(P - YD) \quad (5.21e)$$

$$0 = \dot{E}^2 L^3 \dot{D} + 2D\dot{E}L^3 \ddot{E} + 3D\dot{E}^2 L^2 \dot{L} + 3U^2 \dot{M} \\ + 6MU\dot{U} + 6\frac{N_1}{N_2}(Y\dot{E}DL - PU) \quad (5.21f)$$

$$P = -P_0 U^2 \quad (5.21g)$$

$$(5.21h)$$

The numerical solution is shown in Figure 5.5 for several P_0 . It is found that unless the density of the surrounding fluid is comparable to that of the jet material, drag has little effect of the jet motion or arrest process. The solution for P_0 corresponding to air is indistinguishable from that in vacuum. As P_0 increases to about $\rho_{fluid} \approx \rho$, the drag resistance slowly aids in deformation arrest by removing energy from the jet flow. For rupture to occur, smaller N_1 is required to compensate for drag losses.

5.5 Stretching of the Root in Transverse Beam Deflection

To represent the inertial stretching of a transversely loaded beam at the attachment points, the external loading in equations 5.5 and 5.6 is used to couple reaction forces. To exemplify the coupling behavior, the beam of perfectly plastic material is taken to be represented by an elementary single mode with deflection angle θ . This is

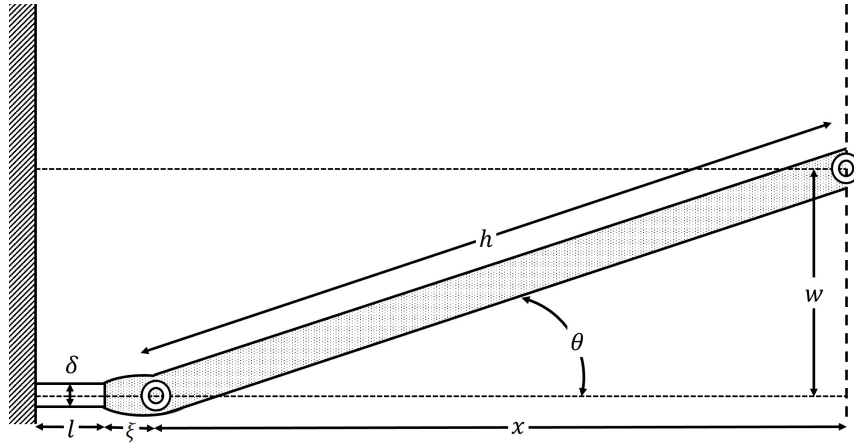


Figure 5.6: Illustration of an single mode beam in phase 3 with tensile stretching at the root

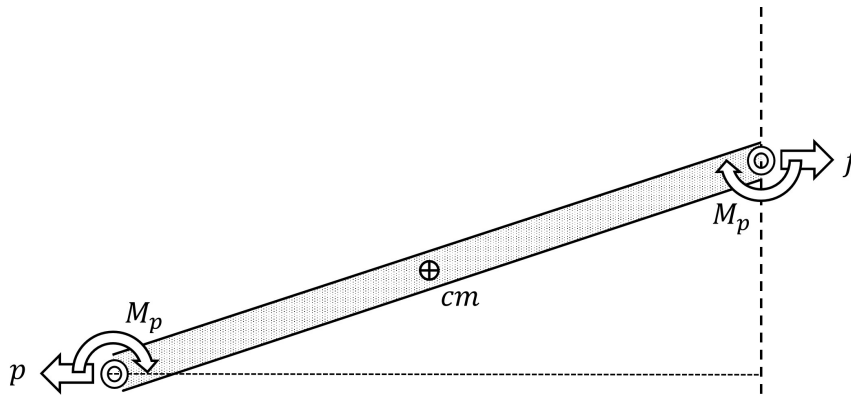


Figure 5.7: Kinetic free-body diagram of an single mode beam with coupling action applied to the root

illustrated in Figure 5.6 with a plastic hinge at the root and at the midpoint symmetry plane. The beam has a constant length h and midpoint deflection w . The horizontal distance between the hinges is x . Suppose stretching of the root starts during phase 3. Time is set, $t = 0$ when the beam has deflected by θ_0 and has an angular velocity $\frac{d\theta}{dt}$. The angular velocity of the beam segment is related to u by

$$x = h \cos(\theta) \tag{5.22}$$

and

$$\frac{dx}{dt} = -u \quad (5.23)$$

The midpoint deflection is simply

$$w = h \sin(\theta) \quad (5.24)$$

The kinetic free-body diagram is shown in Figure 5.7. The center of mass lies at the beam segment center, therefore the angular momentum balance about the midpoint hinge is given by

$$-pw - 2 \operatorname{sgn} \left(\frac{d\theta}{dt} \right) M_p = I_o \frac{d^2\theta}{dt^2} - \rho\delta_0 h \frac{x}{2} \frac{d^2w}{dt^2} \quad (5.25)$$

where M_p is the plastic moment, $M_p = \frac{\delta_0^2}{4} \sigma_y$ that resists rotational motion and $I_o = \frac{1}{12}(4h^2 + \delta_0)$ is the moment of inertia about an end. The function $\operatorname{sgn}()$ is the sign function which is defined as 1 for a positive argument and -1 for a negative argument. Both x and w scale with h . In dimensionless form,

$$X = \cos(\theta) \quad (5.26)$$

and

$$W = \sin(\theta) \quad (5.27)$$

. The relationship between $\frac{dx}{dt}$ and u becomes

$$\dot{X} = -\frac{1}{N_3} U \quad (5.28)$$

where $N_3 = \frac{h}{\delta_0}$. The angular momentum balance scales with M_p . Therefore

$$-4PW - 2 \operatorname{sgn} \left(\dot{\theta} \right) = \frac{4N_3^2 + 1}{3N_1} \ddot{\theta} - 2 \frac{N_3^2}{N_1} X \ddot{W} \quad (5.29)$$

The dimensionless number $R_n = \frac{N_3^2}{N_1}$ has been identified by Zhao [111] as the response number essential for characterizing rigid-plastic beam behavior to dynamic loads.

Numerical solution to the system of equations 5.30 results in the coupled action.

$$\dot{M} = D\dot{Z} \quad (5.30a)$$

$$\dot{M} = -D\dot{L} - L\dot{D} \quad (5.30b)$$

$$U = \dot{E}L \quad (5.30c)$$

$$U = N_2(\dot{L} + \dot{Z}) \quad (5.30d)$$

$$M\dot{U} = \frac{N_1}{N_2}(P - YD) \quad (5.30e)$$

$$0 = \dot{E}^2 L^3 \dot{D} + 2D\dot{E}L^3 \ddot{E} + 3D\dot{E}^2 L^2 \dot{L} + 3U^2 \dot{M} \\ + 6MU\dot{U} + 6\frac{N_1}{N_2}(Y\dot{E}DL - PU) \quad (5.30f)$$

$$X = \cos(\theta) \quad (5.30g)$$

$$\dot{X} = -\frac{1}{N_3}U \quad (5.30h)$$

$$W = \sin(\theta) \quad (5.30i)$$

$$\ddot{\theta} = \frac{3N_1}{4N_3^2 + 1} \left(2\frac{N_3^2}{N_1}X\ddot{W} - 4PW - 2\operatorname{sgn}(\dot{\theta}) \right) \quad (5.30j)$$

Figure 5.8 shows a numerical solution that arrests without rupture. The deflection angle monotonically increases by about 2 degrees until motion ceases. The coupling force, positive for pulling on the plastic zone gradually decreases along with the plastic-strain rate. The cross section reduces to about 0.35.

When rupture occurs, there is residual rotation motion. This is illustrated in Figure 5.9. The coupling force decreases to zero at rupture. The plastic strain-rate increases in an exponential form and tends to infinity and the plastic zone cross section has a sharp drop just prior to rupture.

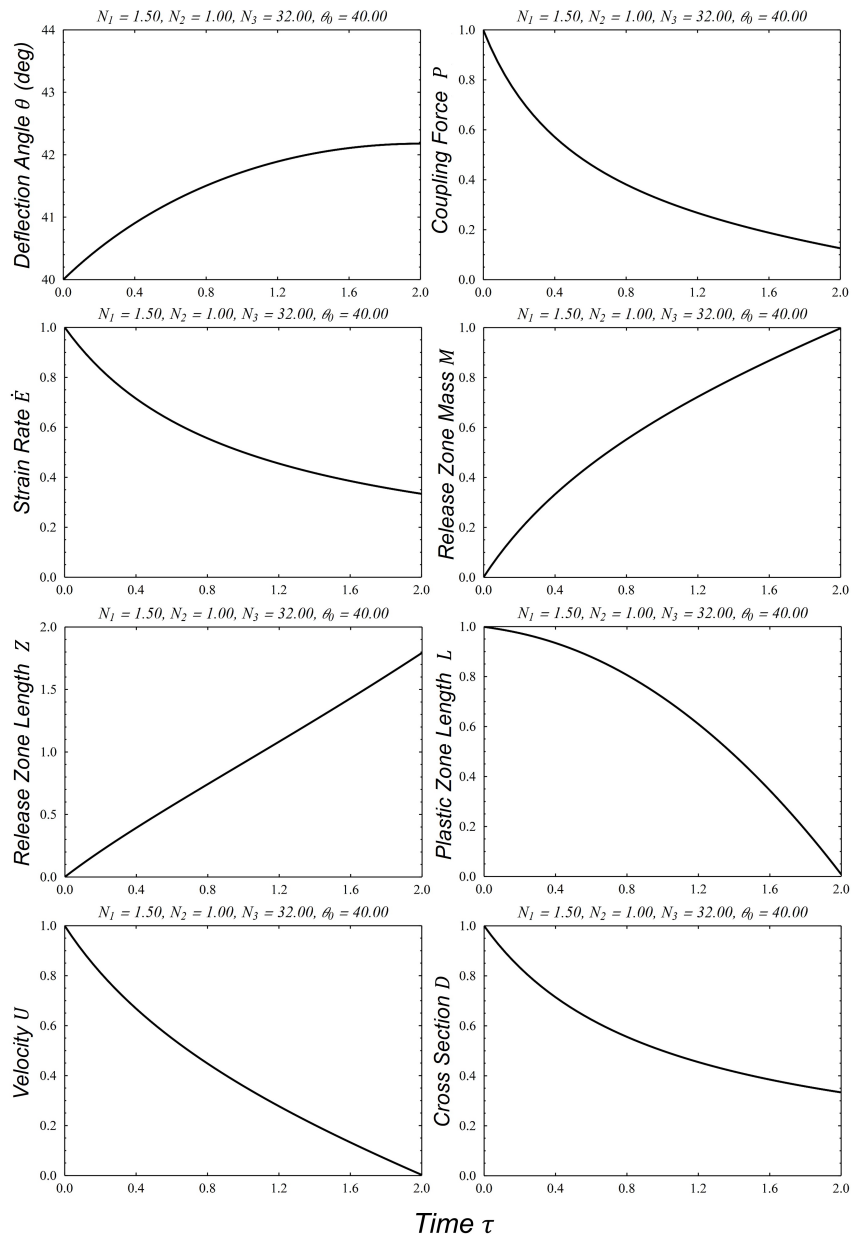


Figure 5.8: Solution of deflecting beam motion fully arresting

5.6 Conclusions

External forces have been applied to the jet tip in the inertially stretching jet undergoing deformation arrest. Closed form solution to a tensile step loading illustrates

Chapter 5. External & Coupling Loads on Deformation Arrest in Ductile Stretching

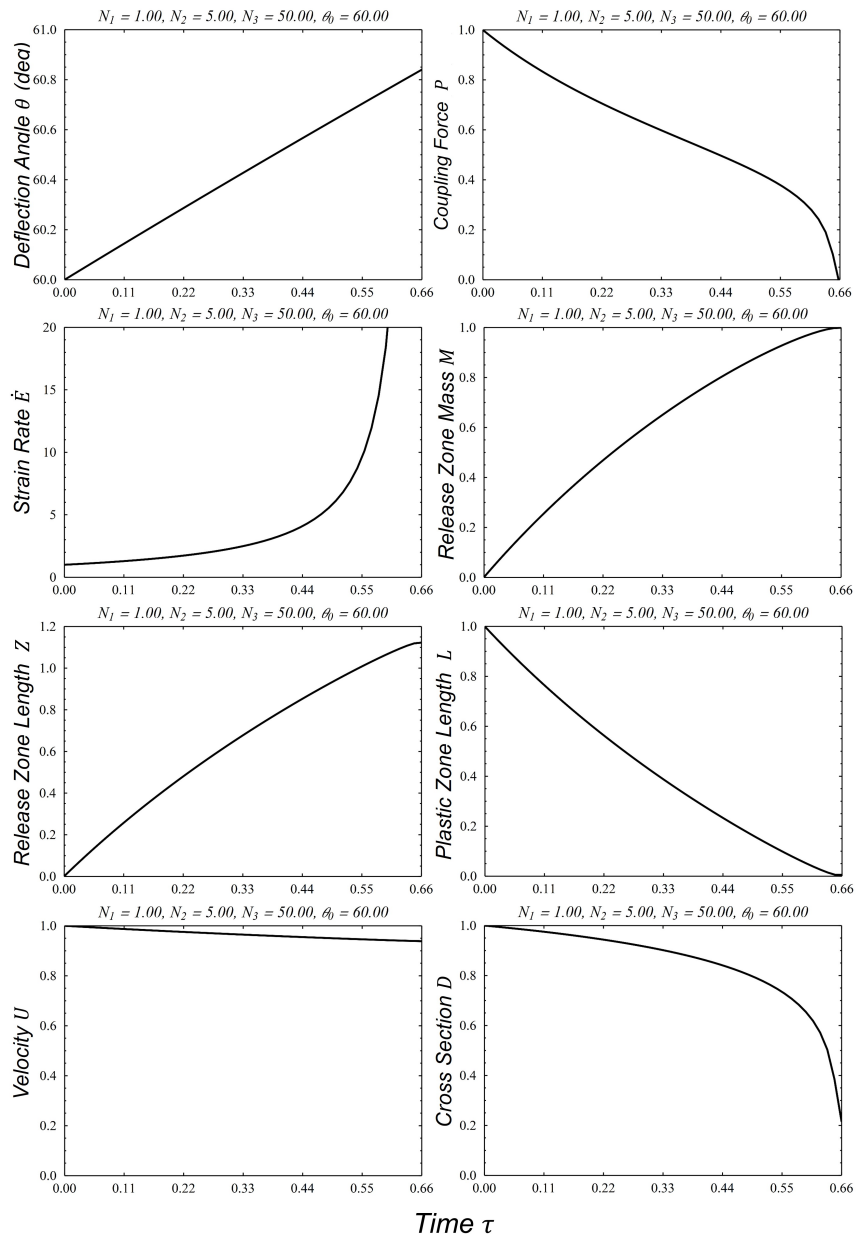


Figure 5.9: Solution of deflecting beam with rupture at the root

the rectangular-hyperbolic relationship between the loading and its impulse on the rupture threshold. The asymptotic limits for minimum impulse at maximum loading and minimum loading at infinite impulse have been derived from first principals.

The asymptote for minimum impulse at maximum loading is found to be dependent on both the jet slender ratio and kinetic energy density to yield strength ratio. The asymptote for the minimum pressure at maximum loading is found to only depend on the kinetic energy density to yield strength ratio. Application of resisting drag forces show little influence on the motion of the jet unless the surrounding fluid density is comparable to that of the jet material. The deformation arrest process realized for the inertial jet has been applied to the tensile stretching of the root with an elementary single mode beam with transverse deflection. Solutions resulting in rupture and full arrest have been shown. Since the solutions display complicated interactions with bifurcations and release-loading cycles, further analysis is warranted. Multi-mode formulations for the transverse beam motions will provide a more accurate representation of real beam behavior. Furthermore, proper initial conditions for the beginning of stretching in phase 3 motion may reduce the complications with choosing valid N_1 , N_2 , N_3 and θ_0 .

Chapter 6

Conclusions

A mathematical theory for deformation arrest in large-strain dynamic plasticity has been proposed. The solutions of the reduced order model provide insight to the physical process governing the vulnerability of ductile structural components such as beams, walls, and blast doors to explosive loadings. Prior analysis required either the use of highly-simplified methods that neglect much of the relevant physics or the use of expensive finite element or shock-code simulation not suited to rapid problem solving and parameter studies. Powerful computers are required to solve the full set of Cauchy momentum equations with strength and state relationships, examples of which are summarized in chapter 2. Yet, predictive rupture conditions were not distinguished in prior publication although decades of research have been performed to obtain these conditions. This dissertation addresses this gap in current understanding and mathematical modeling technique.

6.1 Summary

In chapter 3, an approach has been developed to predictively model the deformation arrest process for the inertially deforming ductile jet where strains can be very large and body shape changes considerably. The solutions are shown to be in excellent agreement with FEA and shock-code simulation. The method employs continuum conservation laws with the propagation of a Mott-Lee release wave over a length where strain-rate and jet cross-section decreases drastically. Moving boundary analysis like those in Stefan-like problems is used to impose compatibility requirements for a continuous body through kinematic constraints. A finite jet body dissipates kinetic energy non-uniformly by internal plastic work. The time-varying plastic zone size is captured with the strain-rate and cross-section shown to be independent of material properties. The velocity pullback phenomenon is demonstrated in solution.

The resulting system of differential-algebraic equations reveals key physical characteristics not yet distinguished. Dimensional analysis uncovers two dimensionless numbers, one related to the plastic velocity increment common in plastic stability analysis and the other with the process time. The closed form solution process leads to theoretical rupture conditions, mass and velocity of the detached particle if rupture occurs, the time for motion to cease as well as the rupture strain. The shape and position of the body at any instant during deformation is obtained from the solution.

In Chapter 4, the Johnson-Cook flow stress equation was used to demonstrate viscoplastic effects on the deformation arrest process. A temperature equation that relates internal plastic work to the homologous temperature is added to the governing system of differential algebraic equations proposed in Chapter 3. A dimensionless number, N_T that relates the conversion of mechanical energy to a temperature-available internal energy gain for melt appears representing the influence of thermal

Chapter 6. Conclusions

softening. It is shown that increased thermal softening reduces the rate of temperature rise. The temperature profile at any instant in time can be obtained from the solution. Strain-rate stiffening is shown to cause an upward shift in yield stress. Due to the logarithmic nature of the strain-rate in the Johnson-Cook equation, the flow-stress drop is minor during deformation. The uniform axial-velocity segment at the jet tip was found to extend into the plastic region. Since the strains are large and increase rapidly, work hardening has the most significant effect. A sharp rise in flow stress occurs followed by a significantly increased velocity pullback effect. When all the effects are combined, work-hardening is dominant and thermal softening effects may become apparent depending on N_T at late time.

Finally, in Chapter 5 external forces have been applied to the release zone in the inertially stretching jet undergoing deformation arrest. Closed form solution to a tensile step loading illustrates the rectangular-hyperbolic relationship between the loading and its impulse on the rupture threshold. Typically, this relationship shape is observed in simplified SDOF systems derived for general structure deformation response. The asymptotic limits for minimum impulse at maximum loading and minimum loading at infinite impulse have been derived from first principals. The asymptote for minimum impulse at maximum loading is found to be dependent on both the jet slender ratio and kinetic energy density to yield strength ratio. The asymptote for the minimum pressure at maximum loading is found to only depend on the kinetic energy density to yield strength ratio. Application of resisting drag forces show little influence on the motion of the jet unless the surrounding fluid density is comparable to that of the jet material. The deformation arrest process realized for the inertial jet has been applied to the tensile stretching of the root of a beam with an elementary single mode in transverse deflection. Solutions resulting in rupture and full arrest have been shown. Multi-mode formulations for the transverse beam motions will provide a more accurate representation of real beam behavior. Furthermore, proper initial conditions for the beginning of stretching in

phase 3 motion may reduce the complications with choosing valid dimensionless system constants.

6.2 Future Work

Due to the general and foundational nature of deformation arrest in dynamically deforming bodies, there are many areas of research that can be influenced by this approach. The solution for the inertial stretching jet leads to particulation phenomena when multiple release zones form and interact with each other. Including the flow stress release from the root of the jet and coupling with the jet tip region may provide a more accurate rupture threshold condition for specific problem scenarios. Allowing a mass in-flow at the root or out-flow at the jet tip may allow for specific solutions to the dynamic extrusion, micro jetting, or wire-drawing problems. The deformation arrest theory can aid in characterizing material behavior in anisotropic plastic flow by applying a flow stress force-vector to the plastic boundary. Furthermore, additional flow stress relationships can be inserted into the governing system that can include other material properties such as brittle rupture strain. Multi-material systems can be incorporated as well. Two and three-dimensional flow stress release can be addressed. Coupling the external loading to reaction forces in general mechanical systems could allow solution to a very large family of unsolved problems in engineering where ductile stretching and dynamic neck retardation occurs. Lastly, reversibility in the arrest process can be studied to aid fundamental understanding of rapid loading resulting in dynamic plastic motions.

Appendices

Appendix A

Example CTH Input File

The following code is an example CTH input file used in the analysis. For more details, see the CTH reference manual [17].

```
*****
*eor* cthin
*****
*
* cth input for Inertially Stretching Jet With Free Fast End
Inertial Jet: Copper, EVPPM model
*
control
  tstop = 1000.0e-6
endcontrol
*
mesh
  block 1 geom=2dc type=e
    x0=0.0
      x1 n=50 w=1.00 ratio=1.0
    endx
    y0=0.0
      y1 n=1250 w=25.00 ratio=1.0
    endy
  endb
endmesh
```

Appendix A. Example CTH Input File

```
*
*****
*
spy
Save("VOLM,VX,VY,J2P,YLD,DENS,M+1,KE,MVOL,PSR,CS");
SaveTime(0, 1e-5);
PlotTime(0, 1e-5);
define main()
{
    pprintf(" PLOT: Cycle=%d, Time=%e\n",CYCLE,TIME);
    XBMirror(ON);
    XLimits(-0.8,0.8);
    YLimits(0,15);
    ImageFormat(1028, 1028);
    DataOut(sprintf("data_%0.6f.dat",TIME),"YLD", "J2P", "M+1", "VY", "KE", "
        MVOL", "PSR", "CS", "DENS");

Image("Misses and Pressure Map",WHITE);
Window(0.05,0,0.8,1);
MatColors(DIMGRAY);
Plot2DMats;
ColorMapRange(0,100,LIN_MAP);
ColorMapClipping(ON,OFF);
DrawColorMap("VX (cm/s)",0.85,0.4,0.99,0.8);
Label(sprintf("Time=%5.1f ~m~s",TIME*1E6));
Right2D;
Plot2D("P");
ColorMapRange(0,7E8,LIN_MAP);
ColorMapClipping(ON,OFF);
DrawColorMap("J2P",0.05,0.4,0.19,0.8);
Left2D;
Plot2D("J2P");
ResetMirrors;
XBMirror(ON);
Draw2DTracers(3);
    Draw2DMatContour;
    EndImage;

Image("YVELOCITY");
Fix1D(0,0,0,20);
VLimits(0,100.00e2,LIN_MAP);
ULabel("Jet Length Distance (cm)");
Label(sprintf("Jet Velocity Profile at %6.2e s.",TIME));
```

Appendix A. Example CTH Input File

```
        Plot1D("VY");
        EndImage;
    }
    SaveHis("GLOBAL");
    HisCycle(0,1);
endspy
*
*****
*
diatoms
    package 'cylinder'
        material 1
        iterations 6
        agraded p1=0,0 p2=0,15
        mvel 0, t1
        insert box
            p1 0.    0.
            p2 0.5  15.
        endinsert
    endpackage
enddiatoms
*
deftable=1
    0.0 0.00
    15.0 150.00e2
enddeftable
*
discard
    material 1
    densl 0.0
    density 1e99
    ton 99.9e-6
    toff 100.8e-6
    dtime 1.0e-6
    ystart 10.0
enddiscard
*****
*
eos
    mat1 ses COPPER
endeos
*
*****
```

Appendix A. Example CTH Input File

```
*
epdata
  vpsave
  matep 1
  eppvm=user yield=7E8 tmelt=1E99 poisson=0.3
ende
*
*****
*
Convct
  interface=high_resolution
endc
*
*****
*
*
edit
  shortt
    time = 00    , dt = 1.0
  ends
*
  longt
    time = 00    , dt = 1.0
  endl
*
ende
*
*****
*
fracts
  pfrac1=-1e30
  pfmix=-1.0e30
  pfvoid=-1.0e30
endf
*
*****
*
boundary
  bhydro
    block 1
      bxbot = 0 , bxtop = 0
      bybot = 0 , bxtop = 0
    endb
```

Appendix A. Example CTH Input File

```
    endh  
endb  
*  
*****
```

Appendix B

Example CTH Output Data Analysis Code

The following Mathematica code extracts the solutions of M , Z , L , D , \dot{E} , and U from the CTH simulation data dumps. Other diagnostic quantities are also extracted. For more detail, see the Mathematica reference manual [61].

```
t = 0.0001;
tmin=t; (* Simulation time minimum *)
dt = 0.000010; (* Simulation output time step *)
tmax = 0.001000; (* Simulation time maximum *)
mtotal=0;
u=0;
c0=0;

r={{0,0}}; (* Length of elastic zone *)
Z={{0,0}}; (* Length of elastic zone *)
Q={{0,0}}; (* Plastic Work with time *)
A={{0,0}}; (* Jet Cross Section with time *)
M={{0,0}}; (* Mass with time *)
U={{0,0}}; (* Particle speed with time *)
L={{0,0}}; (* Distance to elastic/plastic boundary with time *)
```


Appendix B. Example CTH Output Data Analysis Code

```

Y={{0,0}}; (* Distance to elastic/plastic boundary with time *)
L1={{0,0}}; (* Distance to elastic/plastic boundary with time *)
U1={{0,0}}; (* Particle speed with time *)
Ml={{0,0}}; (* Lead Particle Mass with time *)
LZ={{0,0}}; (* Distance to Particle Tip *)
Z1={{0,0}}; (* Length of elastic zone *)
Dl={{0,0}}; (* Neck Diameter with time *)
Rl={{0,0}}; (* Neck Diameter with time *)
KE={{0,0}}; (* Kinetic Energy with time *)
KEy={{0,0}}; (* Kinetic Energy with time *)
LDOT={{0,0}}; (* Change of Distance to elastic/plastic boundary with respect to time
*)
MToT={{0,0}}; (* Total Mass with time *)
KEToT={{0,0}}; (* Kinetic Energy with time *)
Delta={{0,0}}; (* Jet Diameter with time *)

While[t<=tmax ,
r = {{0,0}};
filename="INPUTFILE";
Print[" Reading "<>filename];
Data=Import[filename,"Table"];

{j,n}=Dimensions[Data];j=j-1; (* Get the dimensions of the simulation output table
*)

If[t <= tmin ,
For[i=2, i < j ,
CellMass = Data[[i]][[7]];
mtotal= mtotal+CellMass;
umax = Max[umax, Data[[i]][[8]]];
i++;
];
Yld= Data[[2]][[5]];
c0= Data[[2]][[12]];
];
For[k=2,Data[[k]][[2]]==Data[[k+1]][[2]],k++]; k=k-1; (* Get number of cells in the
simulation x-direction *)

For[o=(j+1)/k-1,Data[[o*k+2]][[10]]==0 ,o--];
o1 = (o+1)*k+2;
CellWidthY = 2*Data[[o*k+2]][[4]];
CellCoordinateY=Data[[o*k+2]][[2]];
CellMassFraction = Data[[o*k+2]][[10]];

```

Appendix B. Example CTH Output Data Analysis Code

```

lz=CellCoordinateY+CellWidthY*CellMassFraction ;
For [o=o, Data [[o*k+2]][[6]] < Data [[o*k+2]][[5]] , o--];
o2=o*k+2;
l=Data [[o*k+2]][[2]];

d=0;
For [i=o2-k, Data [[i]][[2]] == Data [[i+1]][[2]] ,
CellWidthX =2*Data [[i]][[3]];
CellMassFraction = Data [[i]][[10]];
d=d+2*CellWidthX*CellMassFraction ;
i++];

m=0;
u=0;
ke=0;
cntr = 0;
For [i=o2, i<=o1 ,
YLD = Data [[i]][[5]];
J2P = Data [[i]][[6]];
CellYPos = Data [[i]][[2]];
CellXPos = Data [[i]][[1]];
CellMass = Data [[i]][[7]];
CellMatSpeed = Data [[i]][[8]];
CellKE = CellMass*Data [[i]][[9]];

If [YLD>J2P,
cntr++;
ke=ke+CellKE;
m=m+CellMass;
u=u+CellMatSpeed;
If [Data [[i+1]][[10]]==0,
CellMassFraction = Data [[i]][[10]] - 0.5;
If [ r == {{0,0}}, r = {{2*(CellXPos+CellWidthX*CellMassFraction), CellYPos}}, AppendTo[
r, {2*(CellXPos+CellWidthX*CellMassFraction), CellYPos}]]
];
];
i++;
];
If [cntr == 0,
u = umax;
cntr =1;
m = 0;
];

```

Appendix B. Example CTH Output Data Analysis Code

```

AppendTo[r, {0, CellYPos}];
AppendTo[R1, r];
AppendTo[D1, {t-tmin, d}];
AppendTo[U1, {t-tmin, u/cntr}];
AppendTo[M1, {t-tmin, m}];
AppendTo[L1, {t-tmin, l}];
AppendTo[Z1, {t-tmin, lz-1}];

d=0;
For[p=2, Data[[p]][[2]] == Data[[p+1]][[2]],
CellWidthX = 2*Data[[p]][[3]];
CellMassFraction = Data[[p]][[10]];
d=d+2*CellWidthX*CellMassFraction ;
p++; p=p-1;
AppendTo[Delta, {t-tmin, d}];

Print[" Writing CONTOURFILE"];
Export["CONTOURFILE", r, "Table"];
t=t+dt]

l0=L1[[2]][[2]];
u0=U1[[2]][[2]];
d0=Delta[[2]][[2]];
L1=Table[{u0/d0 L1[[i]][[1]], L1[[i]][[2]]/l0}, {i, 2, Floor[(tmax -tmin)/dt]};
Z1=Table[{u0/d0 Z1[[i]][[1]], Z1[[i]][[2]]/l0}, {i, 2, Floor[(tmax -tmin)/dt]};
M1=Table[{u0/d0 M1[[i]][[1]], M1[[i]][[2]]/mtotal}, {i, 2, Floor[(tmax -tmin)/dt]};
U1=Table[{u0/d0 U1[[i]][[1]], U1[[i]][[2]]/u0}, {i, 2, Floor[(tmax -tmin)/dt]};
D1=Table[{u0/d0 D1[[i]][[1]], D1[[i]][[2]]/d0}, {i, 2, Floor[(tmax -tmin)/dt]};
Delta=Table[{u0/d0 Delta[[i]][[1]], Delta[[i]][[2]]/d0}, {i, 2, Floor[(tmax -tmin)/dt
]}}];

Print[" Writing OUTPUTFILE"];
Export["OUTPUTFILE", Table[{d0/u0*M1[[i]][[1]], mtotal*M1[[i]][[2]], l0*L1[[i
]][[2]], l0*Z1[[i]][[2]], u0*U1[[i]][[2]], /4 (d0 Delta[[i]][[2]])^2 (*a0*A[[i
]][[2]]*), c0 (*ketot0*KE[[i]][[2]]*), d0*Delta[[i]][[2]], mtotal, Yld, tmin, tmax}, {i
, 1, Floor[(tmax -tmin)/dt]-1}], "Table"];

```

Appendix C

Example Abaqus Keyword Input

The following code is an abbreviated example Abaqus CAE keyword input set used in the analysis. For more detail, see the Abaqus reference manual [1].

```
**
** PARTS
**
*Part , name=Part-1
*End Part
**
**
** ASSEMBLY
**
*Assembly , name=Assembly
**
*Instance , name=Part-1-1, part=Part-1
*Element , type=CAX4R
*Nset , nset=Set-1, generate
*Elset , elset=Set-1, generate
** Section: Jet Material
**
*Solid Section , elset=Set-1, material=Copper ,
*End Instance
**
```

Appendix C. Example Abaqus Keyword Input

```
*Nset , nset=Set-9, instance=Part-1-1, generate
*Elset , elset=Set-9, instance=Part-1-1, generate
*Nset , nset=Set-10, instance=Part-1-1, generate
*Elset , elset=Set-10, instance=Part-1-1, generate
*Nset , nset=Set-11, instance=Part-1-1, generate
*Elset , elset=Set-11, instance=Part-1-1, generate
*Nset , nset=Set-12, instance=Part-1-1, generate
*Elset , elset=Set-12, instance=Part-1-1, generate
*Nset , nset=Set-13, instance=Part-1-1, generate
*Elset , elset=Set-13, instance=Part-1-1, generate
*Nset , nset=Set-14, instance=Part-1-1, generate
*Elset , elset=Set-14, instance=Part-1-1, generate
*End Assembly

**
** MATERIALS
**
*Material , name=Copper
*Density
  8.94623,
*Elastic
  1.37014e+12, 0.3
*Plastic
  7e+08,0.
**
** BOUNDARY CONDITIONS
**
** Name: BC-1 Type: Symmetry/Antisymmetry/Encastre
*Boundary
Set-9, XSYMM
** Name: BC-2 Type: Displacement/Rotation
*Boundary
Set-10, 2, 2
**
** PREDEFINED FIELDS
**
** Name: Predefined Field-1 Type: Velocity Using Field: Y
Part-1-1.1, 1, 0.
Part-1-1.1, 2, 0.
Part-1-1.2, 1, 0.
Part-1-1.2, 2, 0.
Part-1-1.3, 1, 0.
Part-1-1.3, 2, 0.
Part-1-1.4, 1, 0.
```

Appendix C. Example Abaqus Keyword Input

Part-1-1.4, 2, 0.
Part-1-1.5, 1, 0.
Part-1-1.5, 2, 0.
Part-1-1.6, 1, 0.
Part-1-1.6, 2, 0.
Part-1-1.7, 1, 0.
Part-1-1.7, 2, 0.
Part-1-1.8, 1, 0.
Part-1-1.8, 2, 0.
Part-1-1.9, 1, 0.
Part-1-1.9, 2, 0.
Part-1-1.10, 1, 0.
Part-1-1.10, 2, 0.
Part-1-1.11, 1, 0.
Part-1-1.11, 2, 0.
Part-1-1.12, 1, 0.
Part-1-1.12, 2, 0.
Part-1-1.13, 1, 0.
Part-1-1.13, 2, 0.
Part-1-1.14, 1, 0.
Part-1-1.14, 2, 0.
Part-1-1.15, 1, 0.
Part-1-1.15, 2, 0.
Part-1-1.16, 1, 0.
Part-1-1.16, 2, 0.
Part-1-1.17, 1, 0.
Part-1-1.17, 2, 0.
Part-1-1.18, 1, 0.
Part-1-1.18, 2, 0.
Part-1-1.19, 1, 0.
Part-1-1.19, 2, 0.
Part-1-1.20, 1, 0.
Part-1-1.20, 2, 0.
Part-1-1.21, 1, 0.
Part-1-1.21, 2, 0.
Part-1-1.22, 1, 0.
Part-1-1.22, 2, 0.
Part-1-1.23, 1, 0.
Part-1-1.23, 2, 0.
Part-1-1.24, 1, 0.
Part-1-1.24, 2, 0.
Part-1-1.25, 1, 0.
Part-1-1.25, 2, 0.

Appendix C. Example Abaqus Keyword Input

Part-1-1.26, 1, 0.
Part-1-1.26, 2, 0.
Part-1-1.27, 1, 0.
Part-1-1.27, 2, 0.
Part-1-1.28, 1, 0.
Part-1-1.28, 2, 0.
Part-1-1.29, 1, 0.
Part-1-1.29, 2, 0.
Part-1-1.30, 1, 0.
Part-1-1.30, 2, 0.
Part-1-1.31, 1, 0.
Part-1-1.31, 2, 0.
Part-1-1.32, 1, 0.
Part-1-1.32, 2, 0.
Part-1-1.33, 1, 0.
Part-1-1.33, 2, 0.
Part-1-1.34, 1, 0.
Part-1-1.34, 2, 0.
Part-1-1.35, 1, 0.
Part-1-1.35, 2, 0.
Part-1-1.36, 1, 0.
Part-1-1.36, 2, 0.
Part-1-1.37, 1, 0.
Part-1-1.37, 2, 0.
Part-1-1.38, 1, 0.
Part-1-1.38, 2, 0.
Part-1-1.39, 1, 0.
Part-1-1.39, 2, 0.
Part-1-1.40, 1, 0.
Part-1-1.40, 2, 0.
Part-1-1.41, 1, 0.
Part-1-1.41, 2, 0.
Part-1-1.42, 1, 0.
Part-1-1.42, 2, 0.
Part-1-1.43, 1, 0.
Part-1-1.43, 2, 0.
Part-1-1.44, 1, 0.
Part-1-1.44, 2, 0.
Part-1-1.45, 1, 0.
Part-1-1.45, 2, 0.
Part-1-1.46, 1, 0.
Part-1-1.46, 2, 0.
Part-1-1.47, 1, 0.

Appendix C. Example Abaqus Keyword Input

-
-
-

```
Part -1-1.22771, 1, 0.  
Part -1-1.22771, 2, 9312.48  
Part -1-1.22772, 1, 0.  
Part -1-1.22772, 2, 9312.48  
Part -1-1.22773, 1, 0.  
Part -1-1.22773, 2, 9312.48  
Part -1-1.22774, 1, 0.  
Part -1-1.22774, 2, 9312.48  
Part -1-1.22775, 1, 0.  
Part -1-1.22775, 2, 9312.48  
Part -1-1.22776, 1, 0.  
Part -1-1.22776, 2, 9312.48  
Part -1-1.22777, 1, 0.  
Part -1-1.22777, 2, 9312.48  
Part -1-1.22778, 1, 0.  
Part -1-1.22778, 2, 9312.48  
Part -1-1.22779, 1, 0.  
Part -1-1.22779, 2, 9312.48  
Part -1-1.22780, 1, 0.  
Part -1-1.22780, 2, 9312.48  
Part -1-1.22781, 1, 0.  
Part -1-1.22781, 2, 9312.48  
Part -1-1.22782, 1, 0.  
Part -1-1.22782, 2, 9312.48  
Part -1-1.22783, 1, 0.  
Part -1-1.22783, 2, 9312.48  
Part -1-1.22784, 1, 0.  
Part -1-1.22784, 2, 9312.48  
Part -1-1.22785, 1, 0.  
Part -1-1.22785, 2, 9312.48  
Part -1-1.22786, 1, 0.  
Part -1-1.22786, 2, 9312.48  
Part -1-1.22787, 1, 0.  
Part -1-1.22787, 2, 9312.48  
Part -1-1.22788, 1, 0.  
Part -1-1.22788, 2, 9312.48
```


Appendix C. Example Abaqus Keyword Input

Part -1-1.22789, 1, 0.
Part -1-1.22789, 2, 9312.48
Part -1-1.22790, 1, 0.
Part -1-1.22790, 2, 9312.48
Part -1-1.22791, 1, 0.
Part -1-1.22791, 2, 9312.48
Part -1-1.22792, 1, 0.
Part -1-1.22792, 2, 9312.48
Part -1-1.22793, 1, 0.
Part -1-1.22793, 2, 9312.48
Part -1-1.22794, 1, 0.
Part -1-1.22794, 2, 9312.48
Part -1-1.22795, 1, 0.
Part -1-1.22795, 2, 9312.48
Part -1-1.22796, 1, 0.
Part -1-1.22796, 2, 9312.48
Part -1-1.22797, 1, 0.
Part -1-1.22797, 2, 9312.48
Part -1-1.22798, 1, 0.
Part -1-1.22798, 2, 9312.48
Part -1-1.22799, 1, 0.
Part -1-1.22799, 2, 9312.48
Part -1-1.22800, 1, 0.
Part -1-1.22800, 2, 9312.48
Part -1-1.22801, 1, 0.
Part -1-1.22801, 2, 9312.48
Part -1-1.22802, 1, 0.
Part -1-1.22802, 2, 9312.48
Part -1-1.22803, 1, 0.
Part -1-1.22803, 2, 9312.48
Part -1-1.22804, 1, 0.
Part -1-1.22804, 2, 9312.48
Part -1-1.22805, 1, 0.
Part -1-1.22805, 2, 9312.48
Part -1-1.22806, 1, 0.
Part -1-1.22806, 2, 9312.48
Part -1-1.22807, 1, 0.
Part -1-1.22807, 2, 9312.48
Part -1-1.22808, 1, 0.
Part -1-1.22808, 2, 9312.48
Part -1-1.22809, 1, 0.
Part -1-1.22809, 2, 9312.48
Part -1-1.22810, 1, 0.

Appendix C. Example Abaqus Keyword Input

```
Part-1-1.22810, 2, 9312.48
Part-1-1.22811, 1, 0.
Part-1-1.22811, 2, 9312.48
Part-1-1.22812, 1, 0.
Part-1-1.22812, 2, 9312.48
Part-1-1.22813, 1, 0.
Part-1-1.22813, 2, 9312.48
Part-1-1.22814, 1, 0.
Part-1-1.22814, 2, 9312.48
Part-1-1.22815, 1, 0.
Part-1-1.22815, 2, 9312.48
Part-1-1.22816, 1, 0.
Part-1-1.22816, 2, 9312.48
** -----
**
** STEP: Deformation Arrest
**
** *Step, name="Deformation Arrest", nlgeom=YES
** *Dynamic, Explicit
**   , 0.001
** *Bulk Viscosity
**   0.06, 1.2
**
** ** OUTPUT REQUESTS
**
** *Restart, write, number interval=1, time marks=NO
**
** ** FIELD OUTPUT: F-Output-1
**
** *Output, field, variable=ALL, number interval=100
**
** ** HISTORY OUTPUT: H-Output-1
**
** *Output, history, variable=ALL
** *End Step
```

Appendix D

Example Abaqus-Python Output Analysis Code

The following python code extracts the solutions of M , Z , L , D , \dot{E} , and U from the Abaqus simulation output file. For more detail, see the Abaqus reference manual [1].

```
from odbAccess import *

InputString = input("Case Number: ")
CaseNo = int(InputString)

odb = openOdb(path='JOBNAME' + '.odb')
outputFile = open('FILENAME')

numberofframes = len(odb.steps['Deformation_Arrest'].frames)
numerofelements = len(odb.steps['Deformation_Arrest'].frames[-1].fieldOutputs['S'].
    values)

tmin = odb.steps['Deformation_Arrest'].frames[0].frameValue
tmax = odb.steps['Deformation_Arrest'].frames[-1].frameValue
```

Appendix D. Example Abaqus-Python Output Analysis Code

```
mtot = 0

for j in range(0, numberofframes):
    l = 9999999
    d = 0
    lz = 0
    u = 0
    cntr = 0
    mass = 0
    f1 = odb.steps['Deformation_Arrest'].frames[j]
    time = f1.frameValue
    for i in range(0, numberofelements):
        vonMises = f1.fieldOutputs['S'].values[i].mises
        elementvolume = f1.fieldOutputs['EVOL'].values[i].data
        elementdensity = f1.fieldOutputs['DENSITY'].values[i].data
        yld = f1.fieldOutputs['YIELDS'].values[i].data
        vel = f1.fieldOutputs['V'].values[i].dataDouble[1]
        Ypos = f1.fieldOutputs['COORD'].values[i].dataDouble[1]
        Xpos = f1.fieldOutputs['COORD'].values[i].dataDouble[0]
        if j == 0:
            mtot = mtot + elementvolume*elementdensity
        if vonMises < 0.999*yld:
            cntr = cntr + 1
            u = u + vel
            l = min(l, Ypos)
            lz = max(lz, Ypos)
            mass = mass + elementvolume*elementdensity
        else:
            d = max(d, Xpos)
    if cntr == 0:
        cntr = 1
    u = u/cntr
    r = d
    d = 2*d
    z = lz-l
    a = 3.141592654*r*r
    print 'time_=%f'%(time)
    print 'mass_=%f'%(mass)
    print 'u_=%f'%(u)
    print 'l_=%f'%(l)
    print 'z_=%f'%(z)
    print 'd_=%f'%(d)
```

Appendix D. Example Abaqus-Python Output Analysis Code

```
        outputFile.write( '%f %f %f %f %f %f %f %f %f %f %f\n' %(time, mass, l, z,
            u, a, 0.0, d, mtot, yld, tmin, tmax))
print 'tmin=%f' %(tmin)
print 'tmax=%f' %(tmax)
print 'mtot=%f' %(mtot)

outputFile.close()
```

Appendix E

Example Mathematica DAE Solver

The following Mathematica code solves the system of DAE's with the solutions stored in the variables M , Z , L , DD , EE , and U where DD is the jet cross-section and EE the strain-rate. For more detail, see the Mathematica reference manual [61].

```
eqns = {
M[0]==M0,
DD[0]==1,
U[0]==1,
L[0]==1-Z0,
Z[0]==Z0,
DD'[t]EE[t]^2 L[t]^3 +2DD[t]EE[t]L[t]^3 EE'[t]+3DD[t]EE[t]^2 L[t]^2 L'[t]+ 3M'[t]U[t]
]^2+6M[t]U[t]U'[t]+6 N1/N2 EE[t]DD[t]L[t]==0, (* Energy Equation *)
0== M'[t]+L'[t]DD[t]+L[t]DD'[t], (* Mass Balance *)
M'[t]== DD[t]Z'[t], (* Accretion Rate Rule *)
U[t]== EE[t]L[t],
1/N2 U[t]== L'[t]+Z'[t],
-(N1/N2) DD[t]==M[t]U'[t] (* Momentem Balance *)
};
vars={
M[t],
Z[t],
L[t],
```

Appendix E. Example Mathematica DAE Solver

```
DD[t],  
EE[t],  
U[t]  
};
```

```
s=NDSolve[eqns, vars, {t, 0, tmax }, PrecisionGoal->8, AccuracyGoal->8];
```

```
M=M[t]/.s;  
Z=Z[t]/.s;  
L=L[t]/.s;  
DD=DD[t]/.s;  
EE=EE[t]/.s;  
U=U[t]/.s;
```

References

- [1] Dassault Systemes, *ABAQUS Documentation*, Dassault Systemes, Providence Rhode Island, 2016.
- [2] Abrahamson, G.R., and Lindberg, H.E., *Peak Load-Impulse Characterization of Critical Pulse Loads in Structural Dynamics, Nuclear Engineering and Design*, 37, pp. 35-46, 1976.
- [3] Abrate, S., Castanie, B., and Rajapakse, D.S.Y., *Dynamic Failure of Composite and Sandwich Structure*, Springer Netherlands, 2013.
- [4] Alexiandes, V., Soloman, A.D., *Mathematical Modeling of Melting and Freezing Proceses*, Taylor and Francis, 1993.
- [5] Algazin, S.D., Lenskii, V. S., “Analytical Investigation of the Unloading Wave”, *PMM*, 40(2), pp. 327-336, 1976.
- [6] Alves, M., Jones N., “Impact failure of beams using damage mechanics: Part IAnalytical model”, *Int. J. Impact Engen*, 27(8), pp. 837-861, 2002.
- [7] Anandavalli, N., Lakshmanan, N., Rajasankar, J., and Prakash, A., “Numerical Studies on Blast Loaded Steel-Concrete-Steel Composite Panels”, *JCES*, 1(3), pp. 102-108, 2012.
- [8] Babkin, A.V., Ladov, S.V., Marinin, V.M. and Fedorov, S.V., “Characteristics of Inertially Stretching Shaped-Charge Jets in Free Flight”, *Journal of Applied Mechanics and Technical Physics*, Vol. 38 (2), 1997.
- [9] Babkin, A.V., Ladov, S.V., Marinin, V.M. and Fedorov, S.V., “Regularities of the Stretching and Plastic Failure of Metal Shaped-Charge Jets”, *Journal of Applied Mechanics and Technical Physics*, Vol. 40 (4), 1999.

References

- [10] Bonora, N., Testa, G., Ruggiero, A., Lannitti, G., Mortazavi, N., Hornqvist, M., “Numerical Simulation of Dynamic Tensile Extrusion Test of OFHC Copper”, *J. Dynamic Behavior Mater.*, Vol. 1 (2), pp. 136-152, 2015.
- [11] Cao, F., Cerreta, E.K., Trujillo, C.P., Gray III, G.T., “Dynamic Tensile Extrusion Response of Tantalum”, *Acta Materialia*, 56, pp. 5804-5817, 2008.
- [12] Carta, G., Stiochino, F., “Theoretical Models to Predict the Flexural Failure of Reinforced Concrete Beams Under Blast Loads”, *Engineering Structures*, 49, pp. 306-315, 2013.
- [13] Chakraborty, S., Shaw, A., Banerjee, B., “An Axisymmetric Model for Taylor Impact Test and Estimation of Metal Plasticity”, *Proc. R. Soc. A*, 471, 2015.
- [14] Clifton, R.J., “Elastic-Plastic Boundaries in Combined Longitudinal and Torsional Plastic Wave Propagation ”, *J. Appl. Mech.*, 35(4), pp. 782-786, 1968.
- [15] Clifton, R.J., Ting, T.C.T., “The Elastic-Plastic Boundary in One-Dimensional Wave Propagation ”, *J. Appl. Mech.*, 35(4), pp. 812-814, 1968.
- [16] Cormie, D., Mays, G., Smith, P., *Blast Effects on Buildings, 2nd Edition*, London: ICE Publishing, 2009.
- [17] Sandia National Laboratories., *CTH User’s Manual and Input Instructions*, Version 11, Sandia National Laboratory, Albuquerque New Mexico, 2014.
- [18] Dastjerdi, A.K., Naghdabadi, R., Arghavani, J., “An Energy-Based Approach for Analysis of Dynamic Plastic Deformation of Metals”, *Int. J. Mech. Sciences*, 66, pp. 94-100, 2013.
- [19] Dombrovskii, G.A., “On the Asymptotic Behavior of an Unloading Wave”, *PMM*, 43(1), pp. 144-152, 1979.
- [20] Eakins, D., and Thadhani, N.N., “Analysis of Dynamic Mechanical Behavior in Reverse Taylor Anvil-on-Rod Impact Tests”, *Int. J. Impact Engng*, 34, pp.1821-1834, 2007.
- [21] Elek, P., and Jaramaz, S., “Modeling of Fragmentation of Rapidly Expanding Cylinders”, *Theoret. Appl. Mech.*, Vol. 32 (2), pp. 113-130, 2005.
- [22] Farren, W.S., and Taylor, G.I., “The heat developed during plastic extension of metals”, *Proc. Roy. Soc. London*, A107, pp. 422-451, 1925.
- [23] Foster, J.C., Maudlin, P.J., Jones, S.E., “On the Taylor Test: A Continuum Analysis of Plastic Wave Propagation”, *AIP Conference Proceedings*, 370, pp. 291, 1996.

References

- [24] Gold, V.M., and Baker, E.R., “A Model for Fracture of Explosively Driven Metal Shells”, *Engineering Fracture Mechanics*, 75, pp. 275-289, 2008.
- [25] Grady, D.E. *Fragmentation of Rings and Shells*, New York: Springer, 2006.
- [26] Grady, D.E., Kipp, M.E., Benson, D.A., “Energy and Statistical Effects in the Dynamic Fragmentation of Meta Rings”, *Proceedings of the Conference of the Mechanical Properties of High Rates of Strain*, Inst. Phys. Conf. Ser. No. 70, pp. 315-320, 1984.
- [27] Gray III, G.T., Cerreta, E., Yablinsky, C.A., Addressio, L.B, Henrie, B.L., Sencer, B.H., Burkett, M., Maudlin, P.J., Maloy, S.A., Trujillo, C.P., and Lopez, M.F., “Influence of Shock Prestraining and Grain Size on the Dynamic-Tensile-Extrusion Response of Copper: Experiments and Simulation”, *AIP Conference Proceedings*, 845, 725(2005).
- [28] Guliaev, U.I.P., Lenskii, V. S., “On the Unloading Wave in Materials with Delayed Yielding”, *PMM*, 32(6), pp. 1097-1099, 1968.
- [29] Hamra, L., Demonceau, J.F., Denoel, V., “Pressure-Impulse Diagram of a Beam Developing Non-Linear Membrane Action Under Blast Loading”, *Int. J. Impact. Engr.*, 86 , pp. 188-205, 2015.
- [30] Hawkyard, J.B., “A Theory for the Mushrooming of Flat-Ended Projectiles Impinging on a Flat Rigid Anvil, Using Energy Considerations”, *Int. J. Mech. Sci.*, Vol. 11 , pp. 313-333, 1969.
- [31] Hawkyard, J.B., Eaton, D., and Johnson, W., “The Mean Dynamic Yield Strength of Copper and Low Carbon Steel at Elevated Temperatures From Measurements of the 'Mushrooming' of Flat-Ended Projectiles”, *Int. J. Mech. Sci.*, Vol. 10 , pp. 929-948, 1968.
- [32] Hill, R., Siebel, M.P.L., “On the Plastic Distortion of Solid Bars by Combining Bending and Twisting”, *J. Mech. Phys. and Solids*, 1(3), pp. 207-214, 1953.
- [33] Hirsch, E., “The Mott Fragmentation Model and the V_{pl} Break-up Parameter”, *Propellants, Explosives, Pyrotechnics*, 14, pp. 31-38, 1989.
- [34] Hodge, P.G., “A General Theory of Piecewise Linear Plasticity Based on Maximum Shear”, *J. Mech. Phys. and Solids*, Vol. 5(4), pp.242-260, 1957.
- [35] House, J.W., Lewis, J.C., Gillis, P.P., Wilson, L.L., “Estimation of Flow Stress Under High Rate Plastic Deformation”, *Int. J. Impact Engng*, Vol. 16 (2), pp.189-200, 1995.

References

- [36] Hu, Y.Q., “Application of Response Number for Dynamic Plastic Response of Plates Subjected to Impulse Loading”, *Int. J. Pressure Vessels and Piping*, 77, pp. 711-714, 2000.
- [37] Johnson, G.R., and Cook, W.H., “A Constitutive Model and Data for Metals Subjected to Large Strains, high Strain Rates and High Temperatures”, Proceedings of the 7th International Symposium on Ballistics, pp. 541-547, 1983.
- [38] Johnson, W., *Impact Strength of Materials*, Edward Arnold, 1972.
- [39] Jones, N., “Plastic Failure of Ductile Beams Loaded Dynamically”, *J. Engng for Ind.*, 98(B1), pp. 131-136, 1976.
- [40] Jones, N., *Structural Impact, 2nd Edition*, Cambridge University Press, 2012.
- [41] Jones, S.E., Drinkard, J.A., Rule, W.K., Wilson, L.L., “An Elementary Theory for the Taylor Impact Test”, *Int. J. Impact Engng*, Vol. 21 (1-2), pp. 1-13, 1998.
- [42] Jones, S.E., Foster, J.C., Gillis, P.P., “Impact of Work-Hardening Cylinders on a Rigid Boundary”, *J. Non-Linear Mechanics*, Vol. 19 (6), pp. 575-586, 1984.
- [43] Jones, S.E., and Gillis, P.P., “An Elementary Scaling Law for Rod Impact Specimens”, *Int. J. Impact Engng*, Vol. 4 (3), pp. 195-201, 1986.
- [44] Jones, S.E., and Gillis, P.P., “On the Equation of Motion of the Undeformed Section of a Taylor Impact Specimen”, *J. Appl. Phys.*, 61 (2), pp. 499-502, 1987.
- [45] Jones, S.E., Gillis, P.P., Foster, J.C., Wilson, L.L., “A One-Dimensional, Two-Phase Flow Model for Taylor Impact Specimen”, *J. Eng. Mater. Technol*, 113 (2), pp. 228-235, 1991.
- [46] Jones, S.E., Maudlin, P.J., Foster, J.C., “An Engineering Analysis of Plastic Wave Propagation in the Taylor Test”, *Int. J. Impact Engng*, Vol. 19 (2), pp. 95-106, 1997.
- [47] Karunes, B., and Onat, E.T., “On the Effect of Shear on Plastic Deformation of Beams Under Transverse Impact Loading”, *J. Appl. Mech.*, 27(1), pp. 107-110, 1960.
- [48] Kipp, M.E., and Grady, D.E., “Dynamic Fracture Growth and Interaction in One Dimension”, *J. Mech. Phys. Solids*, Vol. 33 (4), pp. 339-415, 1985.
- [49] Langdon, G.S., Schleyer G.K., “Inelastic Deformation and Failure of Clamped Aluminum Plates Under Pulse Pressure Loading”, *Int. J. Impact Engng*, 28, pp. 1107-1127, 2003.

References

- [50] Lee, E.H., “The Continuum Mechanics Aspect of Material Properties Determination”, *Energetics III*, pp. 85-122, 1967.
- [51] Lee, E.H., and Tupper, S.J., “Analysis of Plastic Deformation in a Steel Cylinder Striking a Rigid Target ”, *J. Appl. Mech.*, 21(1), pp. 63-70, 1954.
- [52] Li, Q.M., “Continuity Conditions at Bending and Shearing Interfaces of Rigid, Perfectly Plastic Structural Elements”, *Int. J. Solids. and Struct.*, 37, pp. 3651-3665, 2000.
- [53] Li, Q.M., “Strain Energy Density Failure Criterion”, *Int. J. Solids. and Struct.*, 38, pp. 6997-7013, 2001.
- [54] Li, Q.M., Jones, N., “On Dimensionless Numbers for Dynamic Plastic Response of Structural Members”, *Archive of Applied Mechanics*, 70, pp. 245-254, 2000.
- [55] Li, Q.M., Meng, H., “Pulse Loading Shape Effects on Pressure-Impulse Diagram of an Elastic-Plastic, Single-Degree-of-Freedom Structural Model”, *Int. J. of Mechanical Sciences*, 44, 2002.
- [56] Li, Q.M., Meng, H., “Pressure-Impulse Diagram for Blast Loads Based on Dimensional Analysis and Single-Degree-of-Freedom Modell”, *J. of Engr. Mechanics*, 28, pp. 87-92, 2002.
- [57] Liew, J., Sohel, K., “Structural Performance of Steel-Concrete-Steel Sandwich Composite Structures”, *Advances in Structural Engineering.*, 2010.
- [58] Lu, G., Yu, T., *Energy Absorbtion of Structures and Materials*, CRC Press, 2003.
- [59] Lu, H., Han., L.H., and Zhao, X.L., “Analytical Behavior of Circular Concrete-Filled Thin-Walled Steel Tubes Subjected to Bending”, *Thin-Walled Structures*, 47(3), pp. 346-358, 2009
- [60] Ludwik, P., “Elemente der Technologischen Mechanik”, *Julius, Springer, Berlin*, pp. 32-38, 1909.
- [61] Wolfram Research, Inc., *Mathematica*, Version 10.4, Wolfram Research Inc., Champaign Illinois, 2016.
- [62] Menkas, S.B., and Opat, H.J., “Broken Beams: Tearing and Shear Failures in Explosively Loaded Clamped Beams”, *Exp. Mech.*, 13(11), pp. 480-486, 1973.
- [63] Mott, N.F., “Fragmentation of Shell Cases”, *Proc. Roy Soc. London, A*, 189, pp. 300-308, 1947.

References

- [64] Neal, B.G., "The Effect of Shear and Normal Forces on the Fully Plastic Moment of a Beam of Rectangular Cross Section", *J. Appl. Mech.*, 28(2), pp. 269-274, 1961.
- [65] Nonaka, T., "Some Interaction Effects in a Problem of Plastic Beam Dynamics. Part 1", *J. Appl. Mech.*, 34, pp. 623-643, 1967.
- [66] Nonaka, T., "Shear and Bending Response of a Rigid-Plastic Beam to Blast-Type Loading", *Ingenieur-Archiv*, 46, pp. 35-52, 1977.
- [67] Nurick, G.N., Shave, G.C., "The Deformation and Tearing of Thin Square Plates Subjected to Impulsive Loads An Experimental Study", *Int. J. Impact Engng*, 18(1), pp. 99-116, 1996.
- [68] Olsen, M.D., Nurick, G.N., and Fagnan, J.R., "Deformation and rupture of blast loaded square plates predictions and experiments", *Int. J. Impact Engng*, 13(2), pp. 279-291, 1993.
- [69] Pack, D.C., "On the Perturbation and Break Up of a Highspeed, Elongating Metal Jet", *J. Appl Phys*, 63, 1864(1988).
- [70] Phillips, A., Wood, E.R., Zabinkski, M.P., Zannis, P., "On the Theory of Plastic Wave Propagation in a Bar - Unloading Waves", *Int. J. Non-Linear Mechanics*, 8, pp. 1-16, 1973.
- [71] Rajendran, R., Lee, J.M., "Blast Loaded Plates", *Marine Structures*, 22, pp. 99-127, 29.
- [72] Rakhmatulin, Kh.A., "On Propagation of Unloading Waves", *Prikl. Mat. Mekh.*, 9(1), pp. 91-100, 1945.
- [73] Romero, L.A., "The Instability of Rapidly Stretching Plastic Jets", *J. Appl Phys*, 65, 3006(1989).
- [74] Shen, W.Q., Jones N., "A Failure Criterion for Beams Under Impulsive Loading", *Int. J. Impact Engen*, 12, pp. 101-121, 1992.
- [75] Shen, W.Q., Jones N., "Dynamic Response and Failure of Fully Clamped Circular Plates Under Impulse Loading", *Int. J. Impact Engen*, 13(2), pp. 259-278, 1993.
- [76] Shi, X.H., Gao, Y.G., "Generalization of Response Number for Dynamic Plastic Response of Shells Subjected to Impulsive Loading", *Int. J. Pressure Vessels and Piping*, 78, pp. 453-459, 2001.

References

- [77] Shorr, B.F., “Analysis of Wave Propagation in Elastic-Plastic Rods of a Variable Cross Section Using Direct Mathematical Modelling”, *Archive of Applied Mechanics*, 65, pp. 537-547, 1995.
- [78] Skobeeb, A.M., “On the Theory of Unloading Waves”, *PMM*, 26(6), pp. 1059-1066, 1962.
- [79] Stronge, W.J., Yu, T.X., *Dynamic Models for Structural Plasticity*, Springer, 1995.
- [80] Symonds, P.S., “Plastic Shear Deformations in Dynamic Load Problems”, *Engineering Plasticity*, ed. J Heyman and F. A. Leckie, *Cambridge University Press*, pp. 647-664, 1968.
- [81] Taylor, G., “The Use of Flat-Ended Projectiles for Determining Dynamic Yield Stress I. Theoretical Considerations”, *Proc. Roy Soc. London, A*, 1038, pp. 289-299, 1948.
- [82] Theobald, M.D., Nurick G.N., “Numerical Investigation of the Response of Sandwich-Type Panels Using Thin-Walled Tubes Subject to Blast Loads”, *Int. J. Impact Engng*, 34, pp. 134-156, 2007.
- [83] Singh, M., Madan, H.R., and Bola, M.S., “Particulation of Metallic Jets Under High Strain Rate”, *Int. J. Impact Engng*, Vol. 15 (5), pp. 699-710, 1994.
- [84] Teeling-Smith, R.G., Nurick, G.N., “The Deformation and Tearing of Thin Circular Plates Subjected to Impulsive Loads”, *Int. J. Impact Engng*, 11(1), pp. 77-91, 1991.
- [85] Stiochino, F., Carta, G., “SDOF Models for Reinforced Concrete Beams Under Impulsive Loads Accounting for Strain Rate Effects”, *Nuclear Engineering Design*, 276, pp. 74-86, 2014.
- [86] Stolz, A., Fischer, K., Roller, C., and Hauser, S., “Dynamic Bearing Capacity of Ductile Concrete Plates Under Blast Loading”, *Int. J. Impact Engng*, 69, pp. 25-38, 2014.
- [87] Theobald, M.D., and Nurick, G.N., “Numerical Investigation of the Response of Sandwich-Type Panels Using Thin Walled Tubes Subjected to Blast Loads”, *Int. J. Impact. Engng*, 34 (1), pp. 134-156, 2007.
- [88] Trujillo, C.P., Martinez, D.T., Burkett, M.W., Escobedo, J.P., Cerreta, E., and Thompson, G., “A Novel Use of PDV for an Integrated Small Scale Test Platform”, *AIP Conference Proceedings*, 1426, 406(2012).

References

- [89] Tuschak, P.A., and Schultz, A.B., “Determination of the Unloading Boundary in Longitudinal Elastic-Plastic Stress Wave Propagation”, *J. Appl. Mech.*, 38(4), pp. 888-894, 1971.
- [90] Walley, S.M., “Shear Localization: A Historical Overview”, *Metallurgical and Materials Transactions A*, 38A, pp. 2629-2654 2007.
- [91] Walsh, J.M., “Plastic Instability and Particulation in Stretching Metal Jets”, *J. Appl Phys*, 56, 1984.
- [92] Wang, Y., Liew, J.Y.R., and Lee, S.W., “Theoretical Models for Axially Restrained Steel-Concrete-Steel Sandwich Panels Under Blast Loading”, *Int. J. Impact Engng.*, 76, pp. 221-231, 2015.
- [93] Wang, B., Lu, G. “Mushrooming of Circular Tubes Under Dynamic Axial Loading”, *Thin-Walled Structures*, 40, pp. 167-182, 2002.
- [94] Wen, H.M., “Deformation and tearing of clamped circular work-hardening plates under impulsive loading”, *Int. J. Pressure Vessels and Piping*, Vol. 75 (1), pp.67-73, 1998.
- [95] Wiffin, A.C., “The Use of Flat-Ended Projectiles for Determining Dynamic Yield Stress II. Tests on Various Metallic Materials”, *Proc. Roy Soc. London, A*, 1038, pp. 289-299, 1948.
- [96] Wlodarczyk, E., Jackowski, A., Sarzynski, S. “Dynamic Behaviour of a Metallic Cylinder Striking a Rigid Target”, *Biuletyn Wojskowej Akademii Technicznej*, 61(4), pp. 75-91, 2012.
- [97] Woodward, R.L., Burman, N.M., Baxter, B.J., “An Experimental and Analytical Study of the Taylor Impact Test”, *Int. J. Impact Engng*, Vol. 15 (4), pp.407-416, 1994.
- [98] Xu, J., Wu, C., and Li, Z.X., “Analysis of Direct Shear Failure Mode for RC Slabs Under External Explosive Loading”, *Int. J. Impact Engen*, 69, pp. 136-148, 2014.
- [99] Xue, z., Vaziri, A., and Hutchinson, J.W., “Material Aspects of Dynamic Neck Retardation”, *J. Mech. and Phys. of Solids*, 56, pp. 93-113, 2008.
- [100] Yao, S., Zhang, D., and Lu, F., “Dimensionless Numbers for Dynamic Response Analysis of Clamped Square Plates Subjected to Blast Loading”, *Arch. Appl. Mech.*, 85, pp. 753-744, 2015.

References

- [101] Yu, T.X., Chen, F.L., “Failure of Plastic Structures Under Intense Dynamic Loading: Modes, Criteria and Thresholds”, *Int. J. Mech. Sciences*, Vol. 42(8), pp. 1537-1554, 2000.
- [102] Yu, T.X., Zhang, L.C. *Plastic Bending: Theory and Applications*, World Scientific Publishing Company, 1996.
- [103] Yuan, C., Qin, Q., and Wang, T.J., “Simplified Analysis of Large Deflection Response of a Metal Sandwich Beam Subjected to Impulsive Loading”, *Acta Mech*, 2015.
- [104] Zaera, R., Arias C., Navarro, C., “Analytical Modelling of Metallic Circular Plates Subjected to Impulsive Loads”, *Int. J. Solids. and Struct.*, 39(3), pp. 659-672, 2002.
- [105] Zaera, R., Rodriguez-Martinez J.A., Vadillo, J., and Fernandez-Saez, J., “Dynamic Necking in Materials with Strain Induced Martensitic Transformation”, *J. Mech. and Phys. of Solids*, 64, pp. 316-337, 2014.
- [106] Zajkan, A., Nikooyiha M., Darvizeh, A., Darvizeh, M., “Effective rigid perfectly plastic models to predict deflection and residual velocity of post local failure motion of impulsively loaded circular plates”, *Int. J. Physical Sciences*, 8(12), pp. 459-480, 2013.
- [107] Zhang, H., and Ravi-Chandar, K., “On the Dynamics of Necking and Fragmentation - I. Real-Time and Post-Mortem Observations in Al 6061-O”, *Int. J. Frac.*, 142, pp. 183-217, 2006.
- [108] Zhang, H., and Ravi-Chandar, K., “On the Dynamics of Necking and Fragmentation - II. Effect of Material Properties, Geometrical Constraints, and Absolute Size”, *Int. J. Frac.*, 150, pp. 3-36, 2008.
- [109] Zang, H., and Ravi-Chandar, K., “Dynamic Fragmentation of Ductile Materials”, *J. Phys. D: Appl. Phys.*, 42, 214010(2009).
- [110] Zhao, Y., “Prediction of Structural Dynamic Plastic Shear Failure by Johnson’s Damage Number”, *Forsch Ingenieurwes*, 63, pp. 349-352, 1998.
- [111] Zhao, Y., “Suggestion of a New Dimensionless Number for Dynamic Plastic Response of Beams and Plates”, *Archive of Applied Mechanics*, 68, pp. 524-538, 1998.
- [112] Zhu, F., Wang, Z., Lu, G., and Nurick, G. “Some Theoretical Considerations on the Dynamic Response of Sandwich Structures Under Impulse Loading”, *Int. J. Impact Engng*, 37, pp. 625-637, 2010.